room temperature to ensure reduction of any disulfide bonds present in the MPA moieties. The reduced polycation solution was then mixed with two-fold excess volume of siRNA (15 μM) dissolved in the same buffer at a mixing residual molar ratio (N/P ratio) of primary amines and amidines in PEG-PLL(MPA) to phosphates in siRNA = 1.7. To facilitate disulfide cross-linking in polyplexes, dialysis (slide-a-lyzer cassette) was performed against 10 mM HEPES buffer (pH 7.4) containing 0.5% v/v DMSO for 2 days, followed by another 2 days of dialysis against 10 mM HEPES buffer (pH 7.4) for removal of DMSO. The obtained PCP solution was mixed with the same volume of sodium silicate solutions (0–60 mM silicate) in 10 mM HEPES buffer (pH 7.4) (a final siRNA concentration: 5 μM), and incubated for 24 h before use. Prior to silica nanogelling, the silicate solutions were prepared by diluting a sodium silicate stock solution (~27% SiO_2) with 10 mM HEPES buffer, and final pH (pH 7.4) was adjusted with HCl. Silica nanogel-coated PCPs are abbreviated as SPCP-X (X represents a silicate concentration (mM) in preparation).

2.4. Dynamic light scattering (DLS) and ζ-potential measurements

DLS and ζ-potential measurements were performed at a temperature of 25 °C and a detection angle of 173° with a Zetasizer Nano ZS instrument (Malvern Instruments Ltd., Worcestershire, UK) equipped with a He-Ne laser ($\lambda = 633$ nm) as the incident beam. For DLS measurements, 20 μL samples of PCP or SPCP in a 10 mM HEPES buffer (pH 7.4) were loaded into a Zen 2112 low-volume cuvette 24 h after preparation. The diffusion coefficient (D_C) of samples, calculated based on the data regarding the decay in the photon correlation function, was converted to the hydrodynamic diameter (D_H) using the Stokes-Einstein equation,

$$D_H = k_B T / 3\pi\eta D_C,$$

where T is the absolute temperature, k_B is the Boltzmann constant, and η is the viscosity of the buffer.

For ζ-potential measurements, 800 μL of sample solutions were put into a folded capillary cell (Malvern Instruments, Ltd.). The ζ-potential (ζ) was calculated from the obtained electrophoretic mobility (v) by applying the Smoluchowski equation

$$\zeta = 4\pi\eta v/\varepsilon,$$

where η is the viscosity of the solvent, v is the electrophoretic mobility, and ε is the dielectric constant of the solvent.

2.5. Scanning transmission electron microscope (STEM)-energy dispersive X-ray (EDX) (STEM-EDX) analysis

STEM-EDX analysis was performed on a 200-keV field-emission gun (FEG) microscope JEOL JEM 2100F (JEOL Ltd., Tokyo, Japan) equipped with a JED-2300T EDX analyzer (JEOL Ltd., Tokyo, Japan). Aqueous aliquots of samples (2 μL) were negatively stained by mixing with 2 μL of uranyl acetate solution (2% w/v in ethanol), then placed on a hydrophilic treated Formvar/carbon-coated copper grid of 400 mesh size (JEOL Ltd., Tokyo, Japan) for 30–45 s before being dried by osmosis against a filter paper at room temperature. Staining was utilized in order to prevent excessive charging and decomposition of the sample under the electron beam. Data were first collected using objective aperture to get bright field (BF) images using an electron beam of 1.5 nm diameter probe with a current of 125 μA, a collection time of 30 s, and 25 scans. For the EDX analyses, the same microscope mode was used, except that objective aperture was eliminated to permit the diffused X-rays to be collected by the EDX detector: 30 mm^2 SDD (silicone drift detector) type with active drift compensation through the microscope control software "Analysis software" (JEOL Ltd., Tokyo, Japan). EDX data were acquired in the approximate 0–10 keV range in 0.01 keV increments. The electron generated X-ray emission peaks occur in the following sequence: C Kα 0.277 keV, N Kα at 0.392 keV, O Kα at 0.525 keV, Si Kα at 1.739 keV, P Kα at 2.013 keV, and S Kα at 2.307 keV. The EDX data were taken as a 256 × 256 pixel, 600 × 600 nm spectrum image with 0.5 ms dwell time per pixel. The EDX spectra were fitted quantitatively using the "Analysis station" software (JEOL Ltd., Tokyo, Japan).

2.6. Agarose gel retardation assay

Polyplex stability (or siRNA release) was examined by agarose gel electrophoresis after incubation with dextran sulfate as a counter polyanion. Samples prepared at 5 μM siRNA (2 μL) was incubated with 10 mM HEPES buffer (pH 7.4) solutions containing 15% glycerol, dextran sulfate (0, 15.6, 31.2, or 46.8 μg/mL), and DTT (0 or 200 mM) (4 μL) for 1 h. Each mixture containing 111 ng siRNA (5 μL) was then loaded onto 1 wt% agarose gel. After electrophoresis at 100 V for 30 min using 1 × TBE running buffer, the gel was stained using ethidium bromide (0.5 mg/L). The gel was visualized at 488 nm for excitation and 620 nm for emission using Typhoon 9410 Gel and Blot Imager (GE Healthcare UK Ltd., England) equipped with the scan control software.

2.7. Time-dependent gene silencing assays

Time-dependent gene silencing activity of polyplexes in cultured cells were determined using AB-2550 Kronos Dio (Atto, Tokyo, Japan), which enables measurement of luminescence emitted from luciferase-expressing cells every 10 min. HeLa-Luc cells were seeded on a 35-mm dish at 25000 cells/well in 2 mL of DMEM containing 10% FBS. After 24 h incubation, the medium was replaced with a fresh medium containing 10% FBS and 100 μM luciferin as a substrate. Each polyplex solution containing 5 μM siGL3 or siSCR was then added to the cells at a final concentration of 100 nM siRNA/well, followed by the luminescence measurement using the Kronos equipment according to the manufacturer's protocol. The results are presented as mean and standard error of the mean obtained from 4 samples.

2.8. Cell viability assay

HeLa-Luc cells were plated onto 96-well plates (10000 cells/well), followed by 24 h incubation in DMEM containing 10% FBS (0.1 mL/well) before replacing with a fresh one. Varying concentrations of SPCP-30 containing siSCR were added to wells at siRNA concentrations ranging between 0 and 500 nM. After 24 h incubation, the cell viability was analyzed using a Cell Counting Kit (CCK)-8 (DOJINDO Laboratories, Kumamoto, Japan), following the manufacturer's protocol. CCK-8 represents a sensitive colorimetric assay for the determination of the number of viable cells based on the reduction of the highly water-soluble tetrazolium salt: WST-8 [2-(2-methoxy-4-nitrophenyl)-3-(4-nitrophenyl)-5-(2,4-disulfophenyl)-2H-tetrazolium, monosodium salt] by dehydrogenases in living cells to give a yellow colored product (formazan). The amount of the formazan dye generated by the activity of dehydrogenases in cells is directly proportional to the number of living cells. The absorbance in each well was measured using a microplate reader (Model 680, BIO-RAD, Hercules, CA, USA). The cell viability in each well was calculated from the obtained values as a percentage of non-treated control wells. The results are presented as mean and standard error of the mean obtained from 8 samples.

2.9. Cellular uptake studies by flow cytometry

The amount of siRNA taken up by HeLa-Luc cells was analyzed by flow cytometry (FCM). HeLa-Luc cells were seeded onto 12-well culture plates (20000 cells/well), followed by 24 h incubation in DMEM containing 10% FBS (1 mL/well). After replacing the medium with fresh one, PCP or SPCP-30 with Cy5-siGL3 was applied to each well at 300 nM siRNA. After 3, 12, and 24 h incubation, cells were rinsed three times with PBS and collected by trypsinization. The collected cells were centrifuged at 1000 g for 2 min and resuspended in PBS. The fluorescence intensity was detected using a BD LSR II instrument (BD Biosciences, Franklin Lakes, NJ, USA) equipped with FACS DIVAsoftware (BD Biosciences). Detection of Cy5 fluorescence was achieved using a 640 nm laser for excitation and a 675 nm long-pass filter for emission. The results are presented as a mean and standard deviation obtained from three samples. For inhibition assays for polyplex endocytosis, the predetermined amount of an endocytic inhibitor, amiloride (1.5 mM), was added to the medium. After 30 min incubation, PCP or SPCP-30 with Cy5-siGL3 was applied to each well at 300 nM siRNA, followed by the similar protocol described above.

2.10. Confocal laser scanning microscope (CLSM) observation

Intracellular distribution studies of PCP and SPCP-30 carrying Cy5-siGL3 were carried out in the presence of a late endosome/lysosome marker, LysoTracker Green. HeLa-Luc cells were plated on a 35 mm glass-based dish at 100000 cells/mL and immersed in DMEM containing 10% FBS. After 24 h incubation, the culture medium was replaced with a fresh one, and the polyplex solution was added at 100 nM siRNA. At 30 min before visualization by LSM780 equipped with the software Zen 2010 with a 63 × objective C-Apochromat (Carl Zeiss, Oberkochen, Germany), Hoechst 33342 (blue) and LysoTracker Green (green) were added at the predetermined concentrations. To evaluate the intracellular distributions of siRNA delivered by polyplexes, CLSM images were taken at different time intervals, and further the colocalization rate of Cy5-siGL3 with the markers was quantified as follows:

$$\text{Colocalization rate}(\%) = \left(\sum \text{Cy5 pixels}_{\text{colocalized}} / \sum \text{Cy5 pixels}_{\text{total}}\right) \times 100,$$

where $\text{Cy5 pixels}_{\text{colocalized}}$ represent the number of Cy5 pixels colocalizing with the marker, and $\text{Cy5 pixels}_{\text{total}}$ represent the number of all Cy5 pixels. The results are presented as mean and standard error of the mean obtained from 25 cells.

2.11. Statistical analysis

The p value was determined by the Student's t-test. The $p < 0.05$ was considered as statistically significant.

3. Results & discussion

3.1. Synthesis of PEG-PLL(MPA)

The synthesis of PEG-PLL(MPA) was performed by the modification of PEG-PLL (Mw of PEG: 12000; DP of PLL: 88) with DTBP in a borate buffer (pH 9.0), in which the primary amino groups of the lysine side chains reacted with imidoester groups contained in DTBP to form amidine groups, with a concomitant release of methanol. An excess molar amount of DTBP (3 equivalents to lysine amines) was used to reduce the polymer–polymer cross-linking, and then unreacted DTBP in the reaction mixture was removed by dialysis. Reduction of the polymer with DTT resulted in cleavage of the internal disulfides and generation of the MPA moiety in the PLL segment. Successful modification of lysine amines with DTBP was confirmed in the ^{1}H NMR spectrum (Supporting Fig. 1), as indicated by the downfield shift of lysine ε-CH_2 groups and the appearance of two methylene peaks corresponding to those found in DTBP. The substitution degree of MPA modification was calculated to be approximately 90% from the peak intensity ratios of the β, γ, and δ-methylene protons of lysine ($-(CH_2)_3-$, δ = 1.3–1.9 ppm) to the protons of mercaptoethyl groups ($HS-(CH_2)_2-$, δ = 2.7–2.9 ppm).

3.2. Preparation of silica nanogel-coated PEGylated cross-linked polyplexes (SPCPs)

Preparation of SPCPs was performed by a two-step protocol. First, platform PCPs were prepared, followed by their silica nanogelling, as illustrated in Fig. 1. As previously reported, the block copolymer PEG-PLL(MPA) can form a core–shell type of cross-linked polyplexes with siRNA at residual molar ratios of [amidines and primary amines in PEG-PLL(MPA)] to [phosphates in siRNA] ranging from 1.1 to 1.9, relatively close to the charge stoichiometric point [28]. Herein, the PCP prepared at the residual molar ratio of 1.7 was selected as a platform for the silica nanogelling, because it possesses slightly positive surface charges (+10.1 mV in ζ-potential) to facilitate the condensation and polymerization of anionic silicates (Table 1).

PCP solutions were mixed with the same volume of sodium silicate solutions (pH 7.4) ranging from 0 to 60 mM to produce SPCPs as well as a control PCP at final concentrations of 0, 5, 10, 20, and 30 mM in silicates and 5 μM in siRNA. Noteworthy, sodium silicate solutions adjusted to a neutral pH contain the readily condensable silicates, $SiO(OH)_3^-$, and orthosilicic acid, $Si(OH)_4$, as major components [35]. As summarized in Table 1, the DLS analysis revealed that the size and PdI of the platform PCP were affected by the silicate concentration in preparation. Particle size drastically increased at 5 mM silicate achieving micron size with a large PdI (>0.3). In contrast, an increase in silicate concentration dramatically reduced particle size, ultimately reaching <150 nm with a lower PdI of ~0.20 (>10 mM silicate). Also, the intensity histograms in DLS revealed a unimodal size distribution of SPCP-30 with a larger size and a slightly larger peak width, compared to that of PCP (Fig. 2). The increase in size, compared to the platform PCP, strongly suggests the generation of the silica nanogel layer surrounding the PCP. The micron sized particle obtained with SPCP-5 are likely the result of secondary aggregate formation between incompletely (or partially) silica-coated polyplexes featuring compromised colloidal stability (or decreased electrostatic and/or steric repulsive force) [35,36,40]. The partial silica nanogelling is suggested by the nearly neutral ζ-potential values of SPCP-5 and SPCP- (~+0.2 mV) (Table 1), which is in between positively charged PCP (~+10 mV) and negatively charged SPCP-20 and SPCP-30 (~−15 mV). The considerably negative ζ-potential values observed for SPCP-20 and SPCP-30 suggest successful silica nanogelling of PCP, as silica nanoparticles possess a significant negative surface charge at a neutral pH [35,36,40]. Apparently, the higher concentrations of silicates in polyplex solutions provided more uniform and thicker silica nanogel layer to the PCP. In this regard, even higher silicate concentrations, *e.g.*, 120 mM silicate for SPCP-60, caused gelation of the entire solutions before mixing with polyplex solutions. Thus, considering the previous result that the silica-coated polyplexes (encapsulating plasmid DNA) prepared at 30 mM silicate achieved the highest gene expression in cultured cells [35], the SPCP-30 formulation was selected as a representative for the following detailed physicochemical and biological characterizations.

Table 1
Hydrodynamic diameter (D_H), polydispersity index (PdI), and ζ-potential of PCP and SPCPs prepared at varying silicate concentrations. The values are presented as mean and standard deviation from three samples except for D_H and PdI of SPCP-5.

Sample	Silicate Conc. (mM)	D_H (nm)	PdI	ζ-Potential (mV)
PCP	0	54.6 ± 1.5	0.09 ± 0.01	+10.1 ± 1.1
SPCP-5	5	15910	0.304	+0.2 ± 0.1
SPCP-10	10	99.2 ± 7.7	0.40 ± 0.01	+0.2 ± 0.2
SPCP-20	20	127.5 ± 2.3	0.19 ± 0.01	−15.1 ± 1.0
SPCP-30	30	139.6 ± 4.1	0.20 ± 0.01	−15.6 ± 1.0

3.3. STEM-EDX analysis

In order to gain direct evidence of silica nanogelling onto PCP, the spatial distribution of the major elemental components in SPCP-30 was investigated by a STEM-EDX analysis and compared to PCP. The STEM-EDX is an advanced microscopic technique that can be used for elemental analysis of flat thin specimen (<10 nm) chiefly in comparison with standard controls for the specimen examined. The BF images were firstly taken for both polyplexes. The obtained BF images display spherical nanoparticles with a diameter of ~30 nm for PCP (Fig. 3A) and ~50 nm for SPCP-30 (Fig. 3B), which are in good agreement with the number-based histograms in DLS measurements (Supporting Fig. 2).

Far away from being a flat thin specimen, such shape and size render the nanoparticles to be considered as thick specimens for EDX, where the point analysis and elemental mapping can be

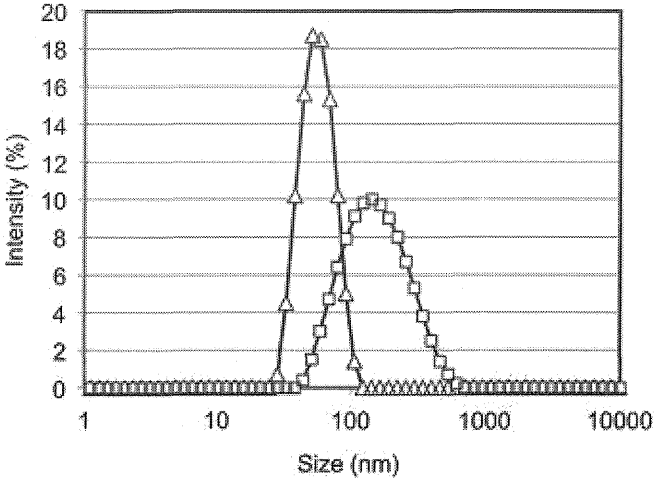

Fig. 2. Intensity-based DLS histograms of PCP (open triangle) and SPCP-30 (open square) (5 μM siRNA).

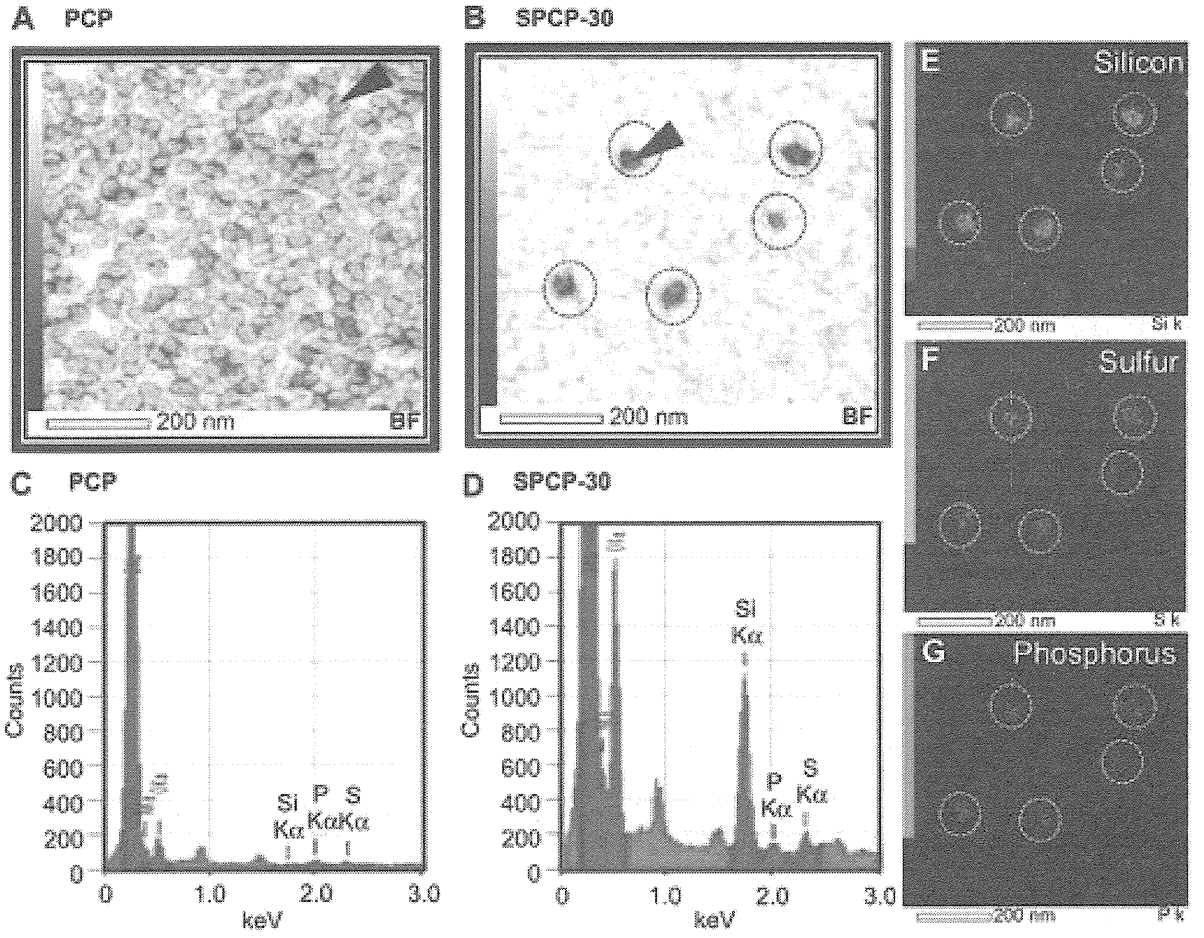

Fig. 3. Bright field (BF) images of PCP (A) and SPCP-30 (B) obtained by STEM, representative EDX spectra of PCP (C) and SPCP-30 (D) taken at the points on the specimen indicated by arrows, and 2-dimensional element maps of SPCP-30 for silicon (E), sulfur (F), and phosphorus (G).

obtained from only the outer surface. Accompanied by the difficulty of preparing standard controls, element quantitative estimation becomes therefore irrelevant in computing the exact composition of the nanoparticles. However, ratios between the different elements can be used to get an approximate estimation about the relative composition of the polyplex surface. Fig. 3C and D display the EDX spectra obtained based on the JEOL 2100F TEM microscope, where the 1.5 nm electron beam was positioned on the center of the nanoparticles, and a total of 20 nanoparticles per each specimen were assessed for the element composition. The 3 major elements that concern the SPCP formulation are: phosphorus contained in siRNA, sulfur contained in PEG-PLL(MPA) side chains, and silicon contained in the silica gel layer. Note that carbon, oxygen, and nitrogen atoms are common in siRNA and the polymer backbone as well as the staining medium used in the specimen preparation; therefore, these signals were not considered for analysis. The comparison between Fig. 3C and D reveals that a relative peak intensity of silicon was obviously magnified in SPCP-30, and also the count ratios of silicon to phosphorus (Si/P) and sulfur (Si/S) show a substantial increase in the silicon content in SPCP-30 (Table 2). Furthermore, the 2-dimensional element maps of SPCP-30 (Fig. 3E–G) clearly display the colocalization of silicon with sulfur and phosphorus as well as the nanoparticles in the BF images. Altogether, these results demonstrate that the silica nanogel layer was deposited onto the PCPs composed of siRNAs and thiolated cationic polymers.

3.4. Reductive environment-responsive stability of PCP and SPCP

Polycations contained in the core of polyplexes may have non-specific interactions with negatively charged biological components to form alternative ion pairs to siRNA phosphates, that is the counter polyion exchange reaction, leading to destabilization of polyplexes or ultimately release of the siRNA payload once exposed to complex biological milieu. This counter polyanion-induced destabilization is a major limitation for effective systemic delivery of siRNA. Hence, the stabilization effect of silica nanogelling against counter polyanion exchange was investigated by agarose gel electrophoresis. This stability assay was executed with or without a reducing reagent DTT, which can imitate intracellular reductive environments, for confirming the reversible stability of polyplexes *via* disulfide bonds. Fig. 4A and B clearly show siRNA release from the PCPs after incubation with dextran sulfate, regardless of DTT. In contrast, SPCP-30 did not show the released siRNA bands in the absence of DTT (Fig. 4A), indicating substantial protective effect of the silica nanogelling to retain siRNA within polyplex structures. On

Table 2
Silicon contents normalized by sulfur and phosphorus on PCP and SPCP-30 in the STEM-EDX analysis. The values are presented as mean and standard error of the mean from 20 nanoparticles.

Sample	Si/S	Si/P
PCP	0.21 ± 0.11	0.28 ± 0.12
SPCP-30	6.56 ± 0.57	31.06 ± 3.53

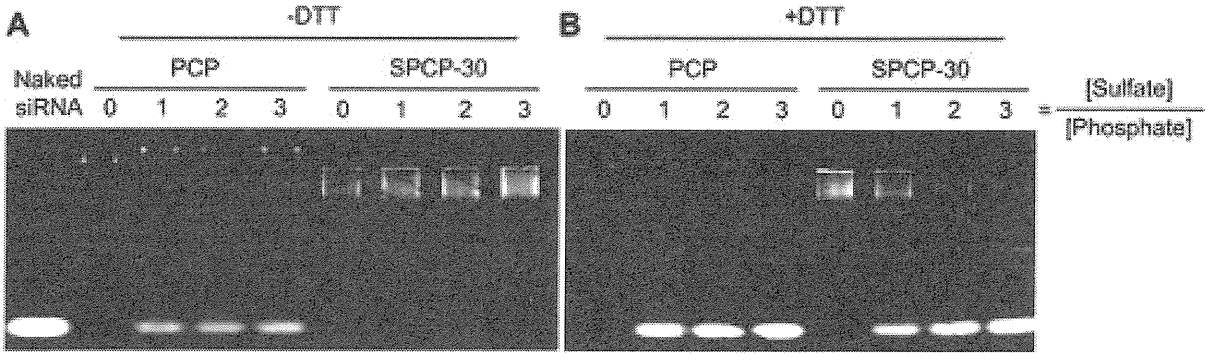

Fig. 4. Gel retardation analysis of PCP and SPCP-30 after incubation with dextran sulfate in the absence of DTT (A) and the presence of DTT (B).

the other hand, the silica nanogelling did not hinder the siRNA release under the reductive environment with DTT (Fig. 4B), confirming that the reductive environment-sensitivity of the PCPs was maintained after the silica nanogelling. Thus, the silica nanogelling demonstrated to suppress the polyplex dissociation synergistically with disulfide cross-links in the polyplex core under the non-reductive condition, while the disulfide cleavage under the reductive condition could lead to the siRNA release from the SPCPs. The mechanism for the reductive environment-sensitivity of SPCPs might be explained by the effect of PEG palisade interfering with silica nanogelling, as follows. In reductive environments, the reducing molecules can reach the polyplex core through pore channels of the silica gel layer, inducing the core disulfide cleavage. This event can render the polyplex core unstable and also the adjacent PEG chains more fluidic, possibly destabilizing the silica gel layer toward the release of enclosed siRNA.

3.5. Time-dependent gene silencing assay

Gene silencing activity of PCP and SPCP-30 was monitored over time in cultured HeLa-Luc cells using AB-2550 Kronos Dio instrument. In this assay, luciferase-based luminescence emitted from HeLa-Luc cells incubated with luciferin (luciferase substrate) was measured as an index for gene silencing activity, and thus siGL3 was used as a target sequence to inhibit luciferase expression, with siSCR as a control. Interestingly, SPCP-30 induced gradual decrease in the relative luciferase expression over 72 h, whereas the decrease observed for PCP leveled off at around 36 h (Fig. 5A). In particular, the significantly enhanced gene silencing activity of SPCP-30, compared to PCP, was obtained from 24 h ($P < 0.05$ at 24 h), and eventually reached twice as high as that of PCP (~29% for SPCP-30 *vs.* ~14% for PCP, $P < 0.05$ at 72 h). Note that significant gene silencing activity was not observed for SPCP-30 carrying siSCR, indicating the sequence-specific gene silencing activity of SPCP-30 carrying siGL3.

Next, the cytotoxicity of SPCP-30 was examined in the same cultured cells using the CCK-8 assay in order to ensure that the enhanced gene silencing activity of SPCP-30 was not associated with an adverse side effect on the cell metabolism or viability. Fig. 5B reveals that almost no cytotoxicity was observed for SPCP-30 carrying siSCR at the tested concentrations of siRNA (100–500 nM). Therefore, the SPCP formulation was demonstrated to enhance the gene silencing activity of PCPs without associated cytotoxicity.

3.6. Cellular uptake studies by flow cytometry

To elucidate the mechanism for the significantly improved gene silencing activity of SPCP-30 compared to PCP, in HeLa-Luc cells (Fig. 5A), the cellular internalization efficiency was compared between the two formulations. In some cases, enhanced transfection efficiency is correlated to enhanced cellular uptake of siRNA through endocytosis as the first event in the cellular delivery process. Thus, the uptake amount of siRNA delivered by PCP and SPCP-30 was quantitatively analyzed by a flow cytometry using Cy5-siRNA. While the cellular uptake of Cy5-siRNA in PCP was more efficient (~3 times higher fluorescence from cells, $p < 0.05$) than that in SPCP-30 at 3 h, longer incubation for 12 and 24 h resulted in

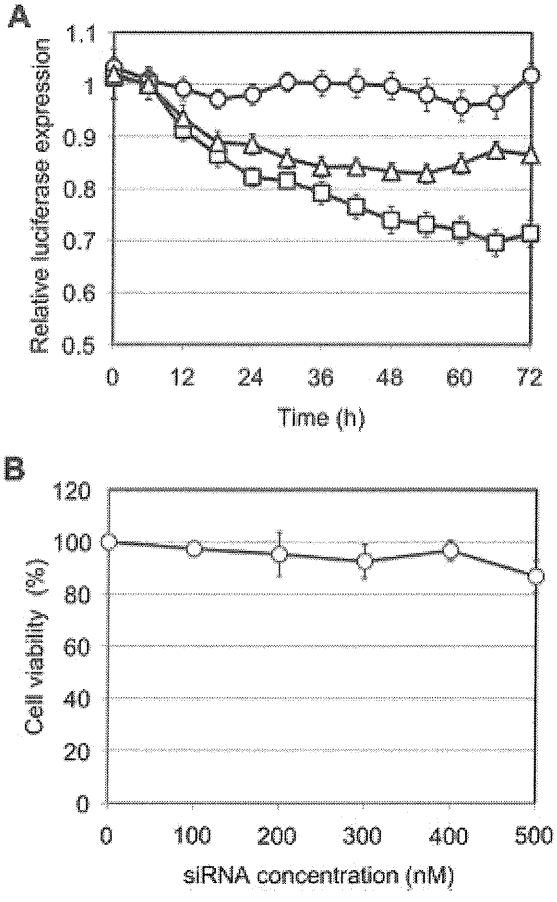

Fig. 5. (A) Time-dependent gene silencing activity of SPCP-30 with siGL3 (open square) in comparison with SPCP-30 with siSCR (open circle) and PCP with siGL3 (open triangle) in cultured HeLa-Luc cells (100 nM siRNA). The luminescence intensity in the cells treated with each polyplex was normalized to that in non-treated cells. Results are expressed mean and standard error of the mean ($n = 4$). (B) Viability of cultured HeLa-Luc cells treated with SPCP-30 carrying siSCR at varying concentrations for 24 h. Results are expressed as mean and standard error of the mean ($n = 8$).

similar uptake of Cy5-siRNA between PCP and SPCP-30 (Fig. 6). Thus, the enhanced gene silencing activity of SPCP-30, which was observed over 3 days, cannot be explained by discrepancies in the amount of siRNA internalized into cells.

3.7. Intracellular trafficking studies by CLSM observation

The enhanced gene silencing activity observed for the SPCP-30 formulation cannot be explained by a difference in cellular uptake, and thus, the mechanism of enhanced activity was further investigated on the subcellular level. Indeed, the endosomal entrapment of polyplexes following the endocytosis was investigated as another critical step in siRNA delivery, as it is believed that the bypass or the escape from the endosomal entrapment (and subsequent lysosomal degradation of siRNA) should be essential for successful RNAi in the cell cytoplasm [31]. Thus, the colocalization of siRNA with the late endosome/lysosome was observed by CLSM imaging using Cy5-siRNA (shown in red). In this experiment, late endosome/lysosome and the cell nuclei in HeLa-Luc cells were stained with LysoTracker Geen (shown in green) and Hoechst 33342 (shown in blue), respectively. After 24 h incubation, the cumulative amount of intracellular Cy5-siRNA was apparently similar between PCP and SPCP-30 (Fig. 7A and B), consistent with the result in the flow cytometric analysis (Fig. 6). Then, colocalization (%) of Cy5-siRNA with the late endosomes/lysosomes was calculated by dividing the colocalized Cy5 signal (yellow) with the total Cy5 signal (yellow and red). This analysis showed that approximately 40% of Cy5-siRNA in SPCP-30 was entrapped in the late endosome/lysosome, which was significantly lower than that in PCP (~68%, $p < 0.01$). This result indicates that SPCP-30-mediated siRNA delivery more efficiently evades the endosomal/lysosomal entrapment, compared to PCP, presumably leading to successful translocation to the cytoplasm toward the enhanced gene silencing activity (Fig. 5A).

Two possible explanations for the lower colocalization rate (or less endosomal entrapment) of SPCP-30 are; i) enhanced endosomal escaping functionality, and ii) modulation of the endocytic pathway toward bypass of the endosomal entrapment. With regard to the endosomal escaping functionality, it has been suggested that deprotonated silanol groups contained in silica, as reflected in the significantly negative ζ-potential of SPCPs (Table 1), can act as a proton acceptor in the acidic late endosome/lysosome (pH < 5.5), possibly facilitating the influx of chloride ions with protons and

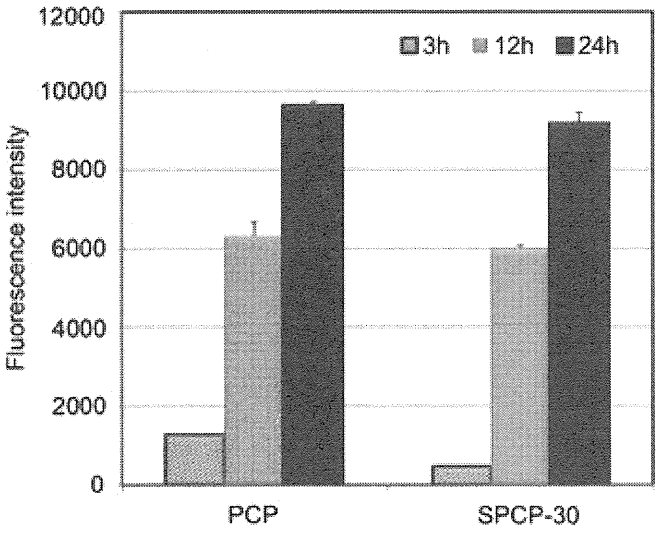

Fig. 6. Cellular uptake of Cy5-siRNA delivered by PCP and SPCP-30 in HeLa-Luc cells (300 nM Cy5-siRNA). Results are expressed as mean and standard error of the mean ($n = 3$).

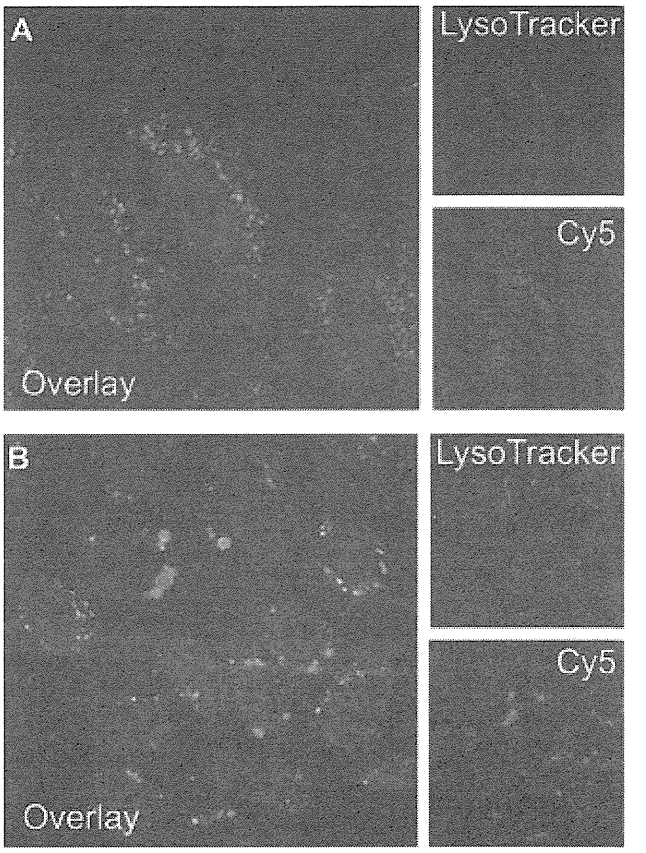

Fig. 7. Intracellular distribution of Cy5-siRNA delivered by PCP (A) and SPCP-30 (B) in HeLa-Luc cells stained with LysoTracker Green and Hoechst 33342 for the late endosome/lysosome and the nuclei, respectively.

increasing the osmotic pressure in the vesicles for the membrane disruption (the proton sponge hypothesis) [31,41,42]. On the other hand, endocytic pathways are also known to affect the intracellular trafficking of endocytosed macromolecules. Among endocytic pathways, macropinocytosis is known as a large-scale fluid endocytic pathway, where the protrusions of highly ruffled invaginations of the plasma membrane extend to engulf a large volume of the surrounding extracellular fluid upon fusing back with themselves or with the plasma membrane to form intracellular uncoated vacuoles, termed macropinosome, with a size of 0.5–10 μm [43]. Interestingly, macropinosomes are reported to be more leaky vesicles compared to the other types of endocytic vesicles, and further not to be necessarily fused with the lysosome [44,45], thereby considered as a potential pathway for enhanced nucleic acid delivery. In addition, several previous studies have reported that silica nanoparticles are significantly uptaken by cells through the macropinocytosis, although other endocytic pathways also contribute to their cellular uptake [46,47].

Accordingly, to elucidate whether SPCP-30 can enter the cells through macropinocytosis, an inhibition assay was performed for HeLa-Luc cells incubated with amiloride, a specific inhibitor of macropinocytosis *via* inhibition of Na^+/H^+ exchange proteins [48]. Considering the fact that cells uptake essential nutrients from external media through endocytic pathways, including macropinocytosis, the inhibition of endocytic pathways might lead to the perturbation of cell homeostasis or ultimately the cell death [49]. A preliminary study suggested that 3 h incubation of the cells with 1.5 mM amiloride should be suitable for minimizing the decrease in the cell viability (data not shown). Treatment of the cells with amiloride significantly decreased the mean fluorescence intensity

from Cy5-siRNA for both PCP and SPCP-30, *i.e.*, the decreasing rate was ~20% for PCP and ~50% for SPCP-30 ($p < 0.05$) in the flow cytometric analysis, indicating that both polyplexes can undergo the macropinocytosis for the cell entry. Nevertheless, the stronger inhibitory effect in SPCP-30 indicates that the silica nanogelling increases a portion of macropinocytosed polyplexes, and also that one of the major endocytic pathways for SPCP-30 is the macropinocytosis. Hence, the assumption that SPCP-30 can evade the endosomal entrapment through the modulated endocytic pathway was consistent with the experimental results.

4. Conclusions

In the present study, the silica nanogelling of PCPs carrying siRNA through silicate condensation was developed for enhanced siRNA carrier stability and functionality. The simple mixing of the platform PCPs with silicates (>10 mM) resulted in successful preparation of silica nanogel-coated PCPs, *i.e.*, the SPCP formulation, featuring a hydrodynamic size of approximately 140 nm with a relatively narrow size distribution (PdI < 0.2) and a negative ζ-potential (~−15 mV), which was in sharp contrast with the positive platform PCPs (~+10 mV) (Table 1). Furthermore, the STEM-EDX analysis directly confirmed the presence of silica on the SPCP surface (Fig. 3). The silica nanogelling substantially suppressed the polyplex dissociation (or siRNA release) induced by the counter polyanion exchange under the non-reductive condition, while allowing the siRNA release under the reductive condition produced with DTT, indicating the reversible stability of SPCPs (Fig. 4). SPCP prepared at 30 mM silicate (SPCP-30) improved the sequence-specific gene silencing activity compared to the platform PCP (Fig. 5A) and also maintained the cell viability (>85%) even at the high concentration tested (500 nM siRNA) against HeLa-Luc cells (Fig. 5B). The enhanced gene silencing of SPCP-30 was apparently correlated with the less endosomal entrapment of the delivered siRNA (Fig. 7), which could be so far explained by two mechanisms; one is the enhanced endosomal escape induced by the proton sponge hypothesis based on deprotonated silanol groups contained in silica, and the other is the modulation in the endocytic pathways, *e.g.*, macropinocytosis, possibly evading the lysosomal degradation of siRNA. In conclusion, this work demonstrates a promising approach to enhance stability and functionality of siRNA-incorporating polyplexes for successful siRNA delivery.

Acknowledgment

This research was financially supported by the Funding Program for World-Leading Innovative R&D on Science and Technology (FIRST) from the Japan Society for the Promotion of Science (JSPS), and also by Izumi Science and Technology Foundation. A part of this work was conducted in Research Hub for Advanced Nano Characterization, The University of Tokyo, supported by the Ministry of Education, Culture, Sports, Science and Technology (MEXT), Japan. N. Gouda acknowledges the fellowship from Ministry of Education, Science, Sports and Culture (MEXT), Japan. We are grateful to Mr. H. Hoshi (JEOL Ltd.) for his technical support.

Appendix A. Supplementary data

Supplementary data related to this article can be found at http://dx.doi.org/10.1016/j.biomaterials.2012.09.077.

References

[1] Elbashir SM, Harborth J, Lendeckel W, Yalcin A, Weber K, Tushl T. Duplexes of 21-nucleotide RNAs mediate interference in cultured mammalian cells. Nature 2001;411(6836):494–8.
[2] de Fougerolles A, Vornlocher HP, Maraganore J, Lieberman J. Interfering with diseases: a progress report on siRNA-based therapeutics. Nat Rev Drug Discov 2007;6(6):443–53.
[3] Burnett JC, Rossi JJ. RNA-based therapeutics: current progress and future prospects. Chem Biol Rev 2012;19(1):60–71.
[4] Fire A, Xu S, Montgomery MK, Kostas SA, Driver SE, Mello CC. Potent and specific genetic interference by double-stranded RNA in *Caenorhabditis elegans*. Nature 1998;391(6669):806–11.
[5] Zimmermann TS, Lee ACH, Akinc A, Bramlage B, Bumcrot D, Fedoruk MN, et al. RNAi-mediated gene silencing in non-human primates. Nature 2006; 441(7089):111–4.
[6] Nakamura Y, Kogure K, Futaki S, Harashima H. Octaarginine-modified multifunctional envelope-type nano device for siRNA. J Control Release 2007; 119(3):360–7.
[7] Akinc A, Zumbuehl A, Goldberg M, Leshchiner ES, Busini V, Hossain N, et al. A combinatorial library of lipid-like materials for delivery RNAi therapeutics. Nat Biotechnol 2008;26(5):561–9.
[8] Semple SC, Akinc A, Chen J, Sandhu AP, Mui BL, Cho CK, et al. Rational design of cationic lipids for siRNA delivery. Nat Biotech 2010;28(2):172–6.
[9] Itaka K, Kanayama N, Nishiyama N, Jang WD, Yamasaki Y, Nakamura K, et al. Supramolecular nanocarrier of siRNA from PEG-based block catiomer carrying diamine side chain with distinctive pKa directed to enhance intracellular gene silencing. J Am Chem Soc 2004;126(42):13612–3.
[10] Kumar P, Wu H, McBride JL, Jung KE, Kim MH, Davidson BL, et al. Transvascular delivery of small interfering RNA to the central nervous system. Nature 2007;448(7149):39–45.
[11] Meyer M, Philipp A, Oskuee R, Schmidt C, Wagner E. Breathing life into polycations: functionalization with pH-responsive endosomolytic peptides and polyethylene glycol enables siRNA delivery. J Am Chem Soc 2008;130(11): 3272–3.
[12] Davis ME, Zuckerman JE, Choi CHJ, Seligson D, Tolcher A, Alabi CA, et al. Evidence of RNAi in humans from systemically administered siRNA via targeted nanoparticles. Nature 2010;464(7291):1067–70.
[13] Shimizu H, Hori Y, Kaname S, Yamada K, Nishiyama N, Matsumoto S, et al. siRNA-based therapy ameliorates glomerulonephritis. J Am Soc Nephrol 2010; 21(4):622–33.
[14] Kim HJ, Ishii A, Miyata K, Lee Y, Wu S, Oba M, et al. Introduction of stearoyl moieties into a biocompatible cationic polyaspartamide derivative, PAsp(-DET), with endosomal escaping function for enhanced siRNA-mediated gene knockdown. J Control Release 2010;145(2):141–8.
[15] Schaffert D, Troiber C, Salcher EE, Frohlich T, Martin I, Badgujar N, et al. Solid-phase synthesis of sequence-defined T-, i-, and U-shape polymers for pDNA and siRNA delivery. Angew Chem Int Ed 2011;50(38):8986–9.
[16] Siegwart DJ, Whitehead KA, Nuhn L, Sahay G, Cheng H, Jiang S, et al. Combinatorial synthesis of chemically diverse core-shell nanoparticles for intracellular delivery. Proc Natl Acad Sci U S A 2011;108(32):12996–3001.
[17] Suma T, Miyata K, Ishii T, Uchida S, Uchida H, Itaka K, et al. Enhanced stability and gene silencing ability of siRNA-loaded polyion complexes formulated from polyaspartamide derivatives with a repetitive array of amino groups in the side chain. Biomaterials 2012;33(9):2770–9.
[18] Giljohann DA, Seferos DS, Prigodich AE, Patel PC, Mirkin CA. Gene regulation with polyvalent siRNA-nanoparticle conjugates. J Am Chem Soc 2009;131(6): 2072–3.
[19] Singh N, Agrawal A, Leung AKL, Sharp PA, Bhatia SN. Effect of nanoparticle conjugation on gene silencing by RNA interference. J Am Chem Soc 2010; 132(24):8241–3.
[20] Zheng D, Giljohann DA, Chen DL, Massich MD, Wang XQ, Iordanov H, et al. Topical delivery of siRNA-based spherical nucleic acid nanoparticle conjugates for gene delivery. Proc Natl Acad Sci U S A 2012;109(30):11975–80.
[21] Kakizawa Y, Furukawa S, Kataoka K. Block copolymer-coated calcium phosphate nanoparticles sensing intracellular environment for oligodeoxynucleotide and siRNA delivery. J Control Release 2004;97(2):345–56.
[22] Xia TA, Kovochich M, Liong M, Meng H, Kabehie S, SGeorge S, et al. Polyethyleneimine coating enhances the cellular uptake of mesoporous silica nanoparticles and allows safe delivery of siRNA and DNA constructs. ACS Nano 2009;3(10):3273–86.
[23] Pittella F, Zhang M, Lee Y, Kim HJ, Tockary T, Osada K, et al. Enhanced endosomal escape of siRNA-incorporating hybrid nanoparticles from calcium phosphate and PEG-block charge-conversional polymer for efficient gene knockdown with negligible cytotoxicity. Biomaterials 2011;32(11): 3106–14.
[24] Lee MY, Park SJ, Park K, Kim KS, Lee H, Hahn SK. Targeted-specific gene silencing of layer-by-layer assembled gold-cysteamine/siRNA/PEI/HA nanocomplex. ACS Nano 2011;5(8):6138–47.
[25] Saito G, Swanson JA, Lee KD. Drug delivery strategy utilizing conjugation via reversible disulfide linkages: role and site of cellular reducing activities. Adv Drug Deliv Rev 2003;55(2):199–215.
[26] Kakizawa Y, Harada A, Kataoka K. Environment-sensitive stabilization of core-shell structured polyion complex micelle by reversible cross-linking of the core through disulfide bond. J Am Chem Soc 1999;121(48):11247–8.
[27] Matsumoto S, Christie RJ, Nishiyama N, Miyata K, Ishii A, Oba M, et al. Environment-responsive block copolymer micelles with a disulfide cross-linked core for enhanced siRNA delivery. Biomacromolecules 2009;10(1):119–27.
[28] Christie RJ, Miyata K, Matsumoto Y, Nomoto T, Menasco D, Lai TC, et al. Effect of polymer structure on micelles formed between siRNA and cationic block

copolymer comprising thiols and amidines. Biomacromolecules 2011;12(9):3174–85.
[29] Christie RJ, Matsumoto Y, Miyata K, Nomoto T, Fukushima S, Osada K, et al. Targeted polymeric micelles for siRNA treatment of experimental cancer by intravenous injection. ACS Nano 2012;6(6):5174–89.
[30] Kakizawa Y, Kataoka K. Block copolymer micelles for delivery of gene and related compounds. Adv Drug Deliv Rev 2002;54(2):203–22.
[31] Miyata K, Nishiyama N, Kataoka K. Rational design of smart supramolecular assemblies for gene delivery: chemical challenges in the creation of artificial viruses. Chem Soc Rev 2012;41(7):2562–74.
[32] Nomoto T, Matsumoto Y, Miyata K, Oba M, Fukushima S, Nishiyama N, et al. In situ quantitative monitoring of polyplexes and polyplex micelles in the blood circulation using intravital real-time confocal laser scanning microscopy. J Control Release 2011;151(2):104–9.
[33] Mizutani T, Nagase H, Ogoshi H. Silicic acid polymerization catalyzed by amines and polyamines. Chem Lett 1998:133–4.
[34] Coradin T, Durupthy O, Livage J. Interactions of amino-containing peptides with sodium silicate and colloidal silica: a biomimetic approach of silicification. Langmuir 2002;18(6):2331–6.
[35] Miyata K, Gouda N, Takemoto H, Oba M, Lee Y, Koyama H, et al. Enhanced transfection with silica-coated polyplexes loading plasmid DNA. Biomaterials 2010;31(17):4764–70.
[36] Suma T, Miyata K, Anraku Y, Watanabe S, Christie RJ, Takemoto H, et al. A smart multilayered assembly for biocompatible siRNA delivery featuring dissolvable silica. Endosome-disrupting Polycation. Detachable PEG ACS Nano 2012;6(8):6693–705.
[37] Fleming BA. Kinetics of reaction between silicic acid and amorphous silica surfaces in NaCl solutions. J Colloid Interface Sci 1986;110(1):40–64.
[38] Popplewell JF, King SJ, Day JP, Ackrill P, Fifield LK, Cresswell RG, et al. Kinetics of uptake and elimination of silicic acid by a human subject: a novel application of ^{32}Si and accelerator mass spectromerty. J Inorg Biochem 1998;69(3):177–80.
[39] Harada A, Kataoka K. Formation of polyion complex micelles in an aqueous milieu from a pair of oppositely-charged block copolymers with poly(ethylene glycol) segments. Macromolecules 1995;28(15):5294–9.
[40] Kobayashi M, Juillerat F, Calletto P, Bowen P, Borkovec M. Aggregation and charging of colloidal silica particles: effect of particle size. Langmuir 2005;21(13):5761–9.
[41] Boussif O, Lezoualc'h F, Zanta MA, Mergny MD, Scherman D, Demeneix B, et al. A versatile vector for gene and oligonucleotide transfer into cells in culture and in-vivo. Proc Natl Acad Sci U S A 1995;92(16):7297–301.
[42] Slowing I, Vivero-Escoto JL, Wu CW, Lin VSY. Mesoporous silica nanoparticles as controlled release drug delivery and gene transfection carrier. Adv Drug Deliv Rev 2008;60(11):1278–88.
[43] Mercer J, Helenius A. Virus entry by macropinocytosis. Nat Cell Biol 2009;11(5):510–20.
[44] Wadia JS, Stan RV, Dowdy SF. Transducible TAT-HA fusogenic peptide enhances escape of TAT-fusion proteins after lipid raft macropinocytosis. Nat Med 2004;10(3):310–5.
[45] Khalil IA, Kogure K, Futaki S, Harashima H. High density of octaarginine stimulates macropinocytosis leading to efficient intracellular trafficking for gene expression. J Biol Chem 2006;281(6):3544–51.
[46] Zhang YY, Hu L, Yu DH, Gao CY. Influence of silica particle internalization on adhesion and migration of human dermal fibroblasts. Biomaterials 2010;31(32):8465–74.
[47] Meng H, Yang S, Li ZX, Xia T, Chen J, Ji ZX, et al. Aspect ratio determines the quantity of mesoporous silica nanoparticle uptake by a small GTPase-dependent macropinocytosis mechanism. ACS Nano 2011;5(6):4434–47.
[48] Hewlett L, Prescott A, Watts C. The coated pit and macropinocytic pathways serve distinct endosome populations. J Cell Biol 1994;124(5):689–703.
[49] von Gersdorff K, Sanders NN, Vandenbroucke R, De Smedt SC, Wagner E, Ogris M. The internalization route resulting in successful gene expression depends on both cell line and polyethylenimine polyplex type. Mol Ther 2006;14(5):745–53.

LETTER

doi:10.1038/nature12488

Uhrf1-dependent H3K23 ubiquitylation couples maintenance DNA methylation and replication

Atsuya Nishiyama[1], Luna Yamaguchi[1], Jafar Sharif[2], Yoshikazu Johmura[1], Takeshi Kawamura[3], Keiko Nakanishi[4], Shintaro Shimamura[5], Kyohei Arita[6], Tatsuhiko Kodama[3], Fuyuki Ishikawa[7], Haruhiko Koseki[2] & Makoto Nakanishi[1]

Faithful propagation of DNA methylation patterns during DNA replication is critical for maintaining cellular phenotypes of individual differentiated cells[1–5]. Although it is well established that Uhrf1 (ubiquitin-like with PHD and ring finger domains 1; also known as Np95 and ICBP90) specifically binds to hemi-methylated DNA through its SRA (SET and RING finger associated) domain and has an essential role in maintenance of DNA methylation by recruiting Dnmt1 to hemi-methylated DNA sites[6–10], the mechanism by which Uhrf1 coordinates the maintenance of DNA methylation and DNA replication is largely unknown. Here we show that Uhrf1-dependent histone H3 ubiquitylation has a prerequisite role in the maintenance DNA methylation. Using *Xenopus* egg extracts, we successfully reproduce maintenance DNA methylation *in vitro*. Dnmt1 depletion results in a marked accumulation of Uhrf1-dependent ubiquitylation of histone H3 at lysine 23. Dnmt1 preferentially associates with ubiquitylated H3 *in vitro* though a region previously identified as a replication foci targeting sequence[11]. The RING finger mutant of Uhrf1 fails to recruit Dnmt1 to DNA replication sites and maintain DNA methylation in mammalian cultured cells. Our findings represent the first evidence, to our knowledge, of the mechanistic link between DNA methylation and DNA replication through histone H3 ubiquitylation.

Several lines of evidence showing the ability of Uhrf1 to bind modified histone H3 (refs 12–16) and the inability of Dnmt1 to catalyse its reaction on Uhrf1-bound hemi-methylated DNA[12,17] suggest that there may be an intermediate that connects Uhrf1 with Dnmt1 at DNA replication sites. Although direct interaction between Uhrf1 and Dnmt1 has been proposed as a means of recruiting Dnmt1 to hemi-methylated DNA sites[6,18,19], we failed to detect a stable interaction between Uhrf1 and Dnmt1 (Supplementary Fig. 2a–d). Therefore, to elucidate the mechanism underlying cooperation of maintenance DNA methylation and DNA replication by Uhrf1, we first reconstituted maintenance DNA methylation using *Xenopus* interphase egg extracts. After DNA replication, genomic DNA purified from sperm chromatin showed a marked incorporation of a radiolabelled methyl group when *S*-[methyl-^{3}H]-adenosyl-L-methionine was used as a donor, indicating that the sperm DNA was methylated (Fig. 1a). The addition of known replication inhibitors, such as aphidicolin, p27 or geminin, almost completely abolished DNA methylation as well as DNA replication (Fig. 1a, Supplementary Fig. 3a, and data not shown), indicating that DNA-replication-dependent DNA methylation can be reproduced in this *in vitro* cell-free system.

Although neither *Xenopus* (x)Uhrf1 nor xDnmt1 bound to mitotic chromatins, both began binding to chromatin with the kinetics similar to that of xPcna after mitotic extracts were stimulated to initiate DNA replication, suggesting a strong correlation between the chromatin loadings of xUhrf1 and xDnmt1 and DNA replication (Supplementary Fig. 3b, c). Treatment with aphidicolin and p27 abolished the chromatin loading of xDnmt1 and xUhrf1, although a slight loading and DNA-replication-independent binding of xUhrf1 to chromatin was still detectable.

Anti-xUhrf1 serum efficiently depleted xUhrf1 protein in the egg extract (Supplementary Fig. 4a). Depletion of xUhrf1 severely impaired xDnmt1 recruitment to the chromatin and DNA-replication-dependent DNA methylation, although xUhrf1 depletion did not affect DNA replication efficiency and timing when compared with mock depletion (Fig. 1b and Supplementary Fig. 4b, c). Add-back of recombinant human (rh)Uhrf1 partly rescued the recruitment of xDnmt1 to the chromatin and DNA-replication-dependent DNA methylation in xUhrf1-depleted extracts (Supplementary Fig. 4b and 5a). It should be noted that the depletion of xUhrf1 or xDnmt1 from the egg extract as well as mock depletion delayed DNA replication timing (see Supplementary Figs 3a and 4c, d), presumably owing to the dilution of interphase egg extracts by the immunodepletion procedure, which is usually observed in this *in vitro* cell-free system[20]. However, it did not affect the efficiency of DNA replication and chromatin loading of xPcna, indicating that neither xUhrf1 nor xDnmt1 was essential for DNA replication under our experimental condition (Fig. 1b and Supplementary Fig. 4c, d).

xDnmt1 depletion in extracts did not inhibit but rather enhanced xUhrf1 binding to chromatin, presumably owing to the increase in the hemi-methylated DNA region (Fig. 1c). Intriguingly, we detected slower-migrating forms of *Xenopus* histone H3 (xH3) in the xDnmt1-depleted chromatin fraction. These slower-migrating forms were hardly detectable in mock-depleted extracts, presumably owing to the rapid conversion of hemi-methylated DNA to fully methylated DNA by xDnmt1 (see also Fig. 1f). Immunodepletion of xUhrf1 from the extracts completely abolished the appearance of these slower-migrating forms in the xDnmt1-depleted extract (Fig. 1c), although DNA replication was not affected by double depletion of xDnmt1 and xUhrf1 (Supplementary Fig. 4d). Add-back of rhUhrf1 partly rescued the appearance of these slower-migrating forms of xH3 (Supplementary Fig. 5b). A band ladder with a higher molecular weight was detected in anti-H3 immunoprecipitates by anti-ubiquitin antibodies (Fig. 1d). In addition, we added an extreme excess of recombinant His-tagged ubiquitin to the egg extracts. In this case, we expected an upshift of the modified bands of xH3. As shown in Supplementary Fig. 6, an upshift of these bands was indeed apparent. Taken together, the slower-migrating forms that appeared after xDnmt1 depletion were ubiquitylated xH3 (xUbH3). Given that xUhrf1 is required for ubiquitylation of xH3 and that it possesses a RING finger domain (see Fig. 1c and Supplementary Fig. 5b), Uhrf1 is most likely to be an E3 ubiquitin ligase for H3. In agreement with this, Uhrf1 was reported to be able to ubiquitylate H3 *in vitro*[21–23].

Mass spectrometry analyses for xUbH3 in xDnmt1-depleted extracts were performed (Supplementary Fig. 7a). Tandem mass spectrometry (MS/MS) database searches of xUbH3 found one potentially modified

[1]Department of Cell Biology, Graduate School of Medical Sciences, Nagoya City University, 1 Kawasumi, Mizuho-cho, Mizuho-ku, Nagoya 467-8601, Japan. [2]RIKEN Center for Integrative Medical Sciences, 1-7-22 Suehiro, Tsurumi-ku, Yokohama 230-0045, Japan. [3]Laboratory for System Biology and Medicine, RCAST, University of Tokyo, Komaba 4-6-1, Meguro-ku, Tokyo 153-8904, Japan. [4]Department of Perinatology, Institute for Developmental Research, Aichi Human Service Center, 713-8 Kamiya-cho, Kasugai, Aichi 480-0392, Japan. [5]Department of Molecular Medicine and Biochemistry, Akita University Graduate School of Medicine, 1-1-1 Hondo, Akita 010-8543, Japan. [6]Graduate School of Medical Life Sciences, Yokohama City University, 1-7-29, Suehiro-cho, Tsurumi-ku, Yokohama 230-0045, Japan. [7]Department of Gene Mechanisms, Graduate School of Biostudies, Kyoto University, Yoshida-Konoe-cho, Sakyo-ku, Kyoto 606-8501, Japan.

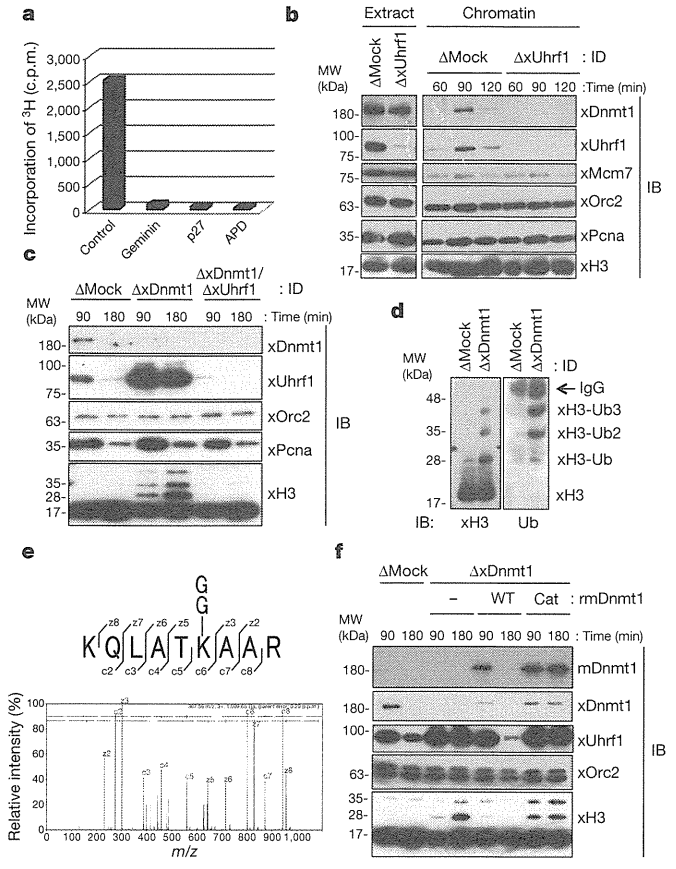

Figure 1 | xUhrf1- and DNA-replication-dependent DNA methylation and ubiquitylation of H3 at lysine 23 in *Xenopus* egg extracts. **a**, Sperm chromatin was incubated with interphase egg extracts containing radiolabelled *S*-[methyl-^{3}H]-adenosyl-L-methionine. His_6–geminin, glutathione *S*-transferase–p27 or aphidicolin (APD, 150 μM) was added to the extracts 10 min before the addition of sperm DNA. After 1 h, sperm DNA was purified from the egg extracts and the incorporation of radioactivity was measured using a scintillation counter. Data shown are representative of three independent experiments. **b**, Interphase egg extracts immunodepleted (ID) with the indicated antiserum were incubated with sperm nuclei. Extracts and sperm chromatin isolated at the indicated times were analysed by immunoblotting (IB) using the indicated antibodies. **c**, Chromatin fractions from interphase extracts immunodepleted with the indicated antibodies were isolated at the indicated times after sperm addition and analysed by immunoblotting. **d**, Chromatin fractions from the indicated immunodepleted extracts were solubilized by MNase and immunoprecipitated with anti-H3 antibodies after treatment with 1% SDS. The resultant immunoprecipitates were subjected to immunoblotting using the indicated antibodies. **e**, The electron transfer dissociation MS/MS spectrum of the xH3 peptide shows ubiquitylation at lysine 23. Detailed information is provided in Methods. **f**, Buffer alone (−), recombinant His_8-tagged wild-type (WT) rmDnmt1, or its catalytic mutant (cat) proteins (10 ng μl^{-1}) were added to xDnmt1-depleted extracts. Chromatin fractions isolated at the indicated times were subjected to immunoblotting using the indicated antibodies.

site at lysine 23 in a trypsin-digested sample[24] (Fig. 1e, see also Supplementary Fig. 7b, c). Lysine 23 in mammalian H3 has been previously reported following a systemic and quantitative proteome analysis of ubiquitylated proteins[25], suggesting that it is present *in vivo* and is physiologically relevant.

xUhrf1-dependent xH3 ubiquitylation in xDnmt1-depleted chromatin fractions was inhibited when DNA replication was blocked by the addition of p27 or aphidicolin (Supplementary Fig. 8), although trace but detectable amounts of xUhrf1 were detected on the chromatin in the presence of p27 or aphidicolin, indicating that ubiquitylation of xH3 by xUhrf1 requires on-going DNA replication.

Either recombinant wild-type or catalytic mutant (C1229S) mouse Dnmt1 (rmDnmt1) proteins[26,27], which were highly homologous to xDnmt1 (91% similarity), were reintroduced in xDnmt1-depleted extracts. Wild-type rmDnmt1 suppressed ubiquitylation of xH3, whereas C1229S failed to do so. Interestingly, wild-type, but not C1229S mutant, rmDnmt1 disappeared on chromatin at 180 min, concomitant with the loss of xUbH3, suggesting that the molecular coupling of deubiquitylation of xUbH3 and rmDnmt1 release from chromatin. These results indicate that recruitment of rmDnmt1 to chromatin per se is insufficient for prevention of xH3 ubiquitylation (Fig. 1f).

Anti-xH3 immunoprecipitates from xDnmt1-depleted extracts specifically bound to xDnmt1, but not to xUhrf1 (Fig. 2a and Supplementary Fig. 9a). The reciprocal experiment using immune-purified xDnmt1, xUhrf1 and xUsp7, a known Dnmt1-binding protein, also revealed that xDnmt1, but not xUhrf1 or xUsp7, bound to ubiquitylated xH3 (Supplementary Fig. 9b and 10a). We then examined whether the interaction of xDnmt1 with xUbH3 was direct. Anti-xH3 immunoprecipitates from xDnmt1-depleted chromatin bound more rmDnmt1 than those from mock-depleted chromatin (Fig. 2b). Specific interaction between rmDnmt1 and xUbH3 was also observed when rmDnmt1 protein was precipitated using anti-Flag antibodies (Fig. 2c). We then performed Far-western blotting analysis using rmDnmt1 protein as a probe. rmDnmt1 specifically bound to xUbH3, but not to other ubiquitylated proteins (see Fig. 2d, middle panel) or polyubiquitin chain per se, showing a preference for diubiquitylated xH3 (Fig. 2d), further confirming the direct and specific binding of Dnmt1 to UbH3. Although xDnmt1 immunoprecipitates bound to nucleosomal xH3 and xUbH3 (Supplementary Fig. 10a), rmDnmt1 preferentially bound to nucleosomal xUbH3 (Fig. 2c) and to monomeric di- or tri-ubiquitylated xH3 on the membrane (Fig. 2d). Although the structural basis underlying Dnmt1 binding to UbH3 is largely unknown, these somewhat distinctive observations might be explained by the possibility that xDnmt1 complexes contain proteins capable of binding to non-ubiquitylated H3 and by the distinct forms of H3, such as nucleosomes, core histones or histone monomer.

The targeting sequence in mouse (m)Dnmt1 that is required for association with replication foci has been previously identified[11]. Wild-type rmDnmt1 effectively bound to xUbH3, whereas a mutant rmDnmt1 lacking association with replication foci (ΔRep; rmDnmt1(Δ325–425)) failed to do so (Fig. 2e). Far-western analysis further confirmed the specific binding of wild-type, but not ΔRep, rmDnmt1 to xUbH3 (Supplementary Fig. 10b).

A similar human (h)Uhrf1-dependent ubiquitylation of hH3 was observed in HeLa cells. When hDnmt1 was depleted, ladders of slow-migrating bands of hH3 were readily detected (Fig. 3a). This ladder was also detected by anti-ubiquitin antibodies (Fig. 3b). However, this hUbH3 was not detected in hDnmt1 and hUhrf1 double-depleted cells (Fig. 3a). As with *Xenopus* egg extract (Supplementary Fig. 8), a ubiquitylation ladder of hH3 was specifically detected in S phase, but not in G1/S phase, chromatin (Supplementary Fig. 11). Notably, the ubiquitylation ladder of hH3 was detected even in the presence of hDnmt1 during normal S phase when hH3 immunoprecipitated from acid-extracted histones was used for immunoblotting (Fig. 3c). When *hDnmt1* was knocked down, the ectopically expressed hUbH3 was detectable by anti-Flag antibody in acid-extracted chromatin proteins from cells expressing wild-type, but not the K23R mutant, hH3 (Fig. 3d), confirming that the ubiquitylation in mammalian cells occurred at the same site as that observed in *Xenopus* extracts. We then examined whether lysine 23 ubiquitylation is prerequisite for Dnmt1 binding to nucleosomes. Ectopically expressed wild-type or K23R hH3 proteins in cells depleted of hDnmt1 were immunoprecipitated and incubated with purified rmDnmt1. The ubiquitylation ladder was only detected in wild-type hH3 precipitates that specifically interacted with rmDnmt1 (Fig. 3e). Taken together with the results using *Xenopus* extracts, Uhrf1-dependent ubiquitylation of H3 at

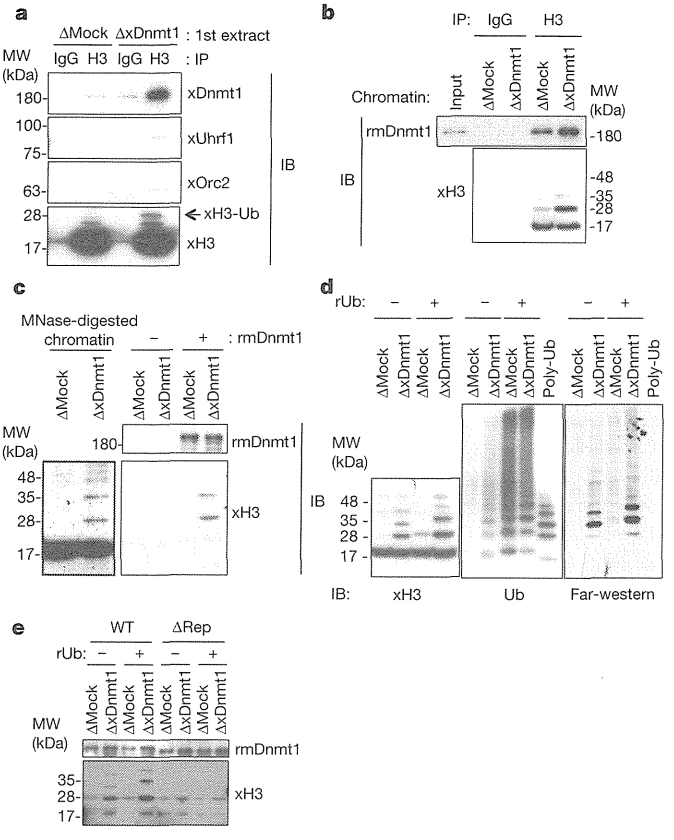

Figure 2 | Dnmt1 preferentially binds to UbH3. a, Chromatin fractions isolated from mock or xDnmt1-depleted extracts (first extracts) were solubilized by MNase and immunoprecipitated with anti-H3 antibodies after treatment with 1% SDS to increase the immunoprecipitation efficiency. The resultant immunoprecipitates were further incubated with untreated interphase extracts and the final immunoprecipitates were subjected to immunoblotting using the indicated antibodies. See also Supplementary Fig. 9a. **b**, Anti-H3 immunoprecipitates from either mock or xDnmt1-depleted chromatin solubilized by MNase were incubated with purified Flag-tagged rmDnmt1. The resultant immunoprecipitates were analysed by immunoblotting using the indicated antibodies. **c**, Flag-tagged rmDnmt1 coupled to beads (+) or control beads (−) was incubated with MNase-digested chromatin isolated from mock or xDnmt1-depleted extracts (left) and the resultant complex was analysed by immunoblotting as in **b** (right). **d**, Far-western blotting analysis of xUbH3 using rmDnmt1 as a probe. Mock or xDnmt1-depleted extracts were incubated with sperm chromatin in the presence or absence of an excess amount of recombinant His_6-ubiquitin (rUb). The chromatin fractions and poly ubiquitin chain (poly-Ub) were electroblotted onto a membrane and probed with anti-H3 antibodies (left), anti-ubiquitin antibodies (middle) or Flag-tagged-purified rmDnmt1 (right). Localization of the probe was carried out by immunoblotting using anti-Flag antibody. **e**, MNase-digested chromatins were incubated with either wild-type or a mutant Flag-tagged rmDnmt1 lacking the first 100 residues of the replication foci targeting sequence (ΔRep; mDnmt1(Δ325–425)). The mixtures were then immunoprecipitated with anti-Flag antibodies and the resultant immunoprecipitates were subjected to immunoblotting using anti-Flag antibodies (top) or anti-H3 antibodies (bottom).

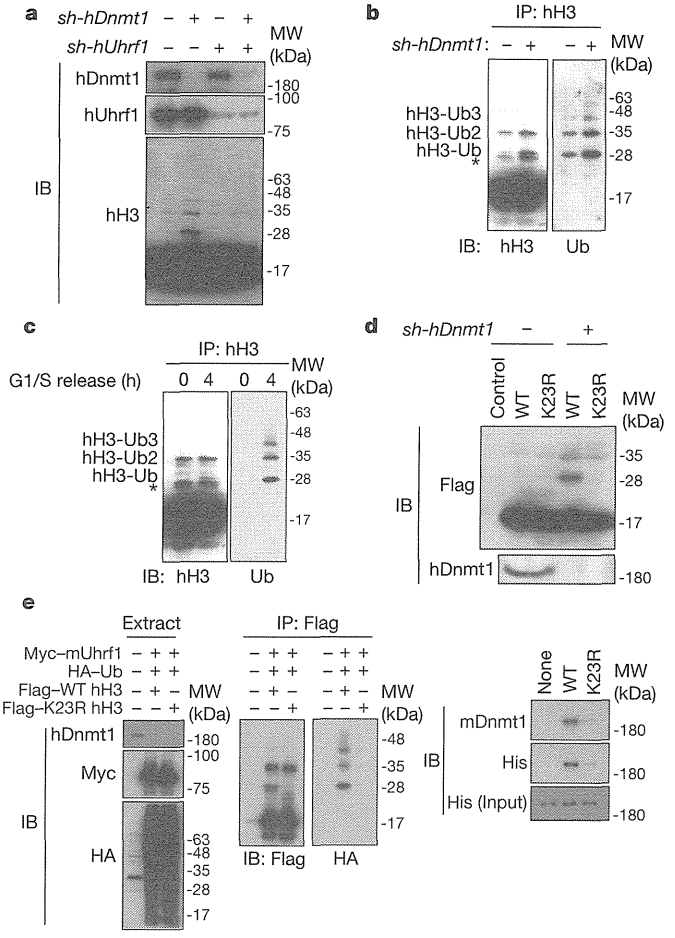

Figure 3 | hUhrf1- and S-phase-dependent ubiquitylation of hH3 at lysine 23 in HeLa cells. a, Extracts from asynchronous HeLa cells knocked down of control (−), *hDnmt1*, *hUhrf1* or *hDnmt1* and *hUhrf1* by their specific shRNAs were subjected to immunoblotting using the indicated antibodies. **b**, Acid-extracted histones from asynchronous HeLa cells knocked down for control (−) or *hDnmt1* were immunoprecipitated with anti-H3 antibodies. The resultant immunoprecipitates were subjected to immunoblotting using anti-H3 (left) and anti-Ub (right) antibodies. Asterisk indicates nonspecific bands. **c**, HeLa cells were synchronized at G1/S and released into S phase. Acid-extracted histones were subjected to immunoprecipitation using anti-H3 antibody. Immunoprecipitates were analysed by immunoblotting using anti-H3 (left) and anti-Ub (right) antibodies. Asterisk indicates nonspecific bands. **d**, *hDnmt1* was knocked down in HeLa cells ectopically expressing either wild-type or K23R mutant Flag-tagged hH3. Cells were collected at 72 h after depletion and histone proteins were isolated by an acid extraction. Cell extracts (bottom) and extracted histones (top) were subjected to immunoblotting using anti-Dnmt1 antibodies and anti-Flag antibodies, respectively. **e**, Ubiquitylation of hH3 at lysine 23 is required for nucleosomal binding of Dnmt1. HeLa cells were transfected with the indicated plasmids and the infected with lentiviruses expressing *sh-hDnmt1*. Cells were collected 72 h after infection and the extracts were immunoprecipitated with anti-Flag antibodies according to the experimental protocols from Abcam as described in Methods. After extensive wash, the immunoprecipitates were incubated with His_8-rmDnmt1 for 1 h at 4 °C. The final precipitates were washed four times and subjected to immunoblotting using the indicated antibodies (right) as well as the extracts (left) and Flag–immunoprecipitates (middle).

lysine 23 seems to be an essential and a general histone mark for recruitment of Dnmt1 in eukaryotes.

Finally, we determined the physiological significance of the E3 ubiquitin ligase activity of Uhrf1. We generated HeLa cells allowing a conditional replacement of endogenous hUhrf1 with either wild-type, SRA (D474G/R489A) or RING finger (C713A/C715A/C716A) mutants of mUhrf1. Wild-type mUhrf1 effectively restored the ability to ubiquitylate hH3 in cells knocked down for endogenous *hUhrf1*, whereas SRA and RING mutants failed to do so (Fig. 4a). Immunohistochemical analysis using *Uhrf1*$^{(\Delta/\Delta)}$ mouse embryonic fibroblasts ectopically expressing wild-type mUhrf1, SRA and RING mutants revealed that both mDnmt1 and mUhrf1 formed nuclear foci during S phase (Fig. 4b). These foci co-localized well with those of mPcna (Supplementary Fig. 12). Again, wild-type mUhrf1 restored the ability of mDnmt1 to form nuclear foci and co-localize with mPcna foci in cells in which endogenous mUhrf1 was deleted. By contrast, although the RING mutant itself formed nuclear foci (Fig. 4b and Supplementary Fig. 12), it failed to restore the ability of mDnmt1 to do so. As expected, the SRA

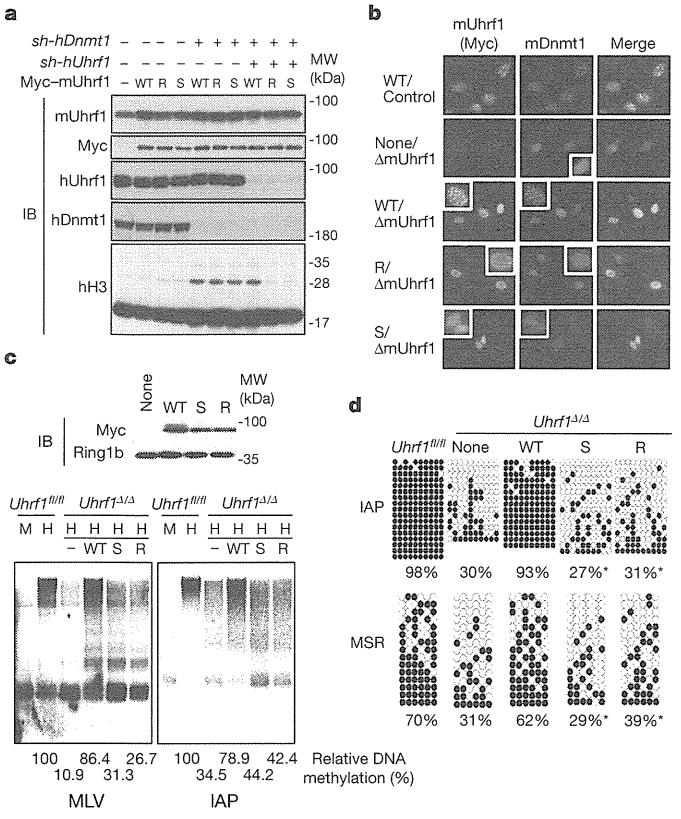

Figure 4 | The RING finger domain of Uhrf1 is crucial for recruitment of Dnmt1 to DNA replication sites and for maintenance of DNA methylation in mammalian cells. **a**, Endogenous *hDnmt1* and/or *hUhrf1* were knocked down from HeLa cells expressing various Myc-tagged mUhrf1 (RING finger domain mutant, R; SRA domain mutant, S) by their specific shRNAs. Cells were then collected 72 h after knockdown and the cell extracts were analysed by immunoblotting using the indicated antibodies. Note that antibodies against hUhrf1 failed to recognize mUhrf1 protein, whereas those against mUhrf1 recognized both proteins. **b**, Endogenous mUhrf1 was deleted from $Uhrf1^{fl/fl}$ mouse embryonic fibroblasts expressing various Myc-tagged mUhrf1 mutants by Cre recombinase expression. Cells were immunostained 72 h after deletion using anti-Myc (Myc–mUhrf1) and anti-Dnmt1 (mDnmt1) antibodies. Inserts show enlarged views of one nucleus. **c**, Endogenous mUhrf1 genes are conditionally deleted by the addition of 4-hydroxytamoxifen from $Uhrf1^{fl/fl}$ embryonic stem cells expressing ER-Cre. Global DNA methylation levels were examined in *Uhrf1* conditional knockout ($Uhrf1^{\Delta/\Delta}$) embryonic stem cells overexpressing the wild-type Uhrf1, the SRA domain mutant (S), the RING domain mutant (R) or control (−) in the presence ($Uhrf1^{\Delta/\Delta}$) or absence ($Uhrf1^{fl/fl}$) of 4-hydroxytamoxifen. The levels of protein expression were analysed by immunoblotting using anti-Myc antibodies and anti-Ring 1b antibodies as a control (top). Genomic DNA (1 μg) was treated with methylation-sensitive HpaII (H) or methylation-insensitive MspI enzyme (M) and analysed by Southern blotting using the indicated probes. Relative DNA methylation was determined by counting radioactivity of the undigested DNA (tops of the gels) and represented as a percentage of DNA undigested by HpaII in $Uhrf1^{fl/fl}$ mouse embryonic stem cells. **d**, Bisulphite DNA sequencing analysis was performed to detect the DNA methylation level in the Gag region of endogenous IAP retrotransposons and MSR (minor satellite repeats) in embryonic stem cells treated as in **c**. Closed circles indicate methylated CpGs and open circles represent unmethylated CpGs. The percentage of DNA methylation (methylation CpGs/total CpGs) is given at the bottom of each panel ($*P < 1 \times 10^{-6}$; compared to wild type).

mutant failed to form nuclear foci or to restore the ability of mDnmt1 to form them. These results suggest that the RING finger domain of mUhrf1 and consequent ubiquitylation of mH3 at lysine 23 are required for the recruitment of mDnmt1 to DNA replication sites. Similar results were also observed when mUhrf1 mutants in the conserved amino acids required for the putative interaction with E2 enzymes were used (Supplementary Fig. 13a–c)[28].

The level of DNA methylation in mouse embryonic stem cells was examined by DNA-methylation-sensitive Southern blotting using intracisternal A-type particle (IAP) and murine leukaemia virus (MLV) regions of the endogenous retrotransposon as probes. Wild-type mUhrf1 or SRA or RING mutants were introduced into $mUhrf1^{fl/fl}$ embryonic stem cells with their comparable expressions (Fig. 4c, top panels). The untreated embryonic stem cells showed a high level of DNA methylation in both IAP and MLV regions of the endogenous retrotransposon. When endogenous mUhrf1 was deleted, their methylation levels were significantly reduced, showing decreased amounts of undigested DNA by HpaII (Fig. 4c). Wild-type mUhrf1 effectively restored the level of global DNA methylation, whereas the RING mutant or the SRA mutant failed to do so. A bisulphite DNA sequencing analysis of the IAP Gag region of the endogenous retrotransposon and minor satellite repeats in mouse embryonic stem cells also demonstrated that wild-type mUhrf1, but not the RING mutant or the SRA mutant, restored the level of DNA methylation (Fig. 4d). Taken together, the results indicate that the RING finger domain of mUhrf1 and consequent ubiquitylation of mH3 at lysine 23 appear to be required for maintaining the level of DNA methylation in mouse embryonic stem cells.

In conclusion, our present results strongly suggest that Uhrf1-dependent ubiquitylation of H3 acts as a platform for the recruitment of Dnmt1 to DNA replication sites (Supplementary Fig. 1). The rapid turnover of H3 ubiquitylation during normal S phase has suggested the presence of a deubiquitylation mechanism coupled with Dnmt1-dependent DNA methylation rather than its proteasomal degradation. In fact, the Dnmt1 complex showed deubiquitylation activity towards ubiquitylated H3 (Supplementary Fig. 14a, b). Thus, it will be of great interest to elucidate the molecular basis underlying the coupling of this deubiquitylation- and Dnmt1-dependent DNA methylation.

METHODS SUMMARY

***Xenopus* egg extracts.** Cytostatic factor (CSF)-arrested and interphase egg extracts were prepared as described[29,30], except that metaphase II-arrested eggs were washed in extraction buffer (EB; 5 mM $MgCl_2$, 100 mM KCl, 20 mM HEPES-KOH, pH 7.5) instead of in 1× Marc's modified Ringers (MMR). Incubation of extracts was carried out at 22 °C.

Immunodepletion. For immunodepletion of *Xenopus* egg extracts, 250 μl of antiserum against xUhrf1 and xDnmt1 were conjugated to 75 μl of protein A agarose (Roche). Twenty-five microlitres of antibody beads were mixed with 100 μl interphase egg extracts and incubated at 4 °C for 1 h. This was repeated three times. For add-back experiments, mDnmt1 wild-type or the C1229S mutant was added to xDnmt1-depleted extracts at 10 ng μl^{-1}.

Monitoring DNA methylation and replication in *Xenopus* egg extracts. DNA methylation was monitored by the incorporation of *S*-[methyl-^{3}H]-adenosyl-L-methionine. Genomic DNA was purified using a Wizard Genomic DNA purification kit (Promega) according to the manufacturer's instructions. The DNA replication efficiency was determined as described previously[20].

Wild-type and mutant Uhrf1-expressing mouse embryonic stem cell cloning. Six micrograms of linearized pCAG-IRES-Puro plasmid containing either a Myc-tagged wild type, an SRA domain mutant (D474G, R489A) or a RING domain mutant (C713A,C715A,C716A) Uhrf1 complementary DNA were transfected into $Uhrf1^{fl/fl}$ embryonic stem cells using FuGENE HD transfection reagent (Roche Applied Science, no. 6366244). Stable clones were selected by puromycin (1 mg ml^{-1}) treatment.

Global DNA methylation analysis and bisulphite DNA sequencing. Genomic DNA was purified from embryonic stem cells using an AllPrep DNA/RNA mini kit according to the supplier's protocol. Genomic DNA was treated with HpaII or MspI and analysed by methylation-sensitive Southern blotting using MLV or IAP as probes. For bisulphite DNA sequencing analysis, genomic DNAs were treated with sodium bisulphite using an EpiTect bisulphite kit. The Gag region of the IAP and MSR retrotransposons was amplified from the bisulphite-treated genomic DNA using the specific primers. PCR products were cloned and sequenced.

Full Methods and any associated references are available in the online version of the paper.

Received 20 November 2012; accepted 18 July 2013.
Published online 8 September 2013.

1. Bird, A. DNA methylation patterns and epigenetic memory. *Genes Dev.* **16,** 6–21 (2002).

2. Jones, P. A. & Liang, G. Rethinking how DNA methylation patterns are maintained. *Nature Rev. Genet.* **10,** 805–811 (2009).
3. Alabert, C. & Groth, A. Chromatin replication and epigenome maintenance. *Nature Rev. Mol. Cell Biol.* **13,** 153–167 (2012).
4. Margueron, R. & Reinberg, D. Chromatin structure and the inheritance of epigenetic information. *Nature Rev. Genet.* **11,** 285–296 (2010).
5. Probst, A. V., Dunleavy, E. & Almouzni, G. Epigenetic inheritance during the cell cycle. *Nature Rev. Mol. Cell Biol.* **10,** 192–206 (2009).
6. Bostick, M. *et al.* UHRF1 plays a role in maintaining DNA methylation in mammalian cells. *Science* **317,** 1760–1764 (2007).
7. Sharif, J. *et al.* The SRA protein Np95 mediates epigenetic inheritance by recruiting Dnmt1 to methylated DNA. *Nature* **450,** 908–912 (2007).
8. Arita, K., Ariyoshi, M., Tochio, H., Nakamura, Y. & Shirakawa, M. Recognition of hemi-methylated DNA by the SRA protein UHRF1 by a base-flipping mechanism. *Nature* **455,** 818–821 (2008).
9. Avvakumov, G. V. *et al.* Structural basis for recognition of hemi-methylated DNA by the SRA domain of human UHRF1. *Nature* **455,** 822–825 (2008).
10. Hashimoto, H. *et al.* The SRA domain of UHRF1 flips 5-methylcytosine out of the DNA helix. *Nature* **455,** 826–829 (2008).
11. Leonhardt, H., Page, A. W., Weier, H. U. & Bestor, T. H. A targeting sequence directs DNA methyltransferase to sites of DNA replication in mammalian nuclei. *Cell* **71,** 865–873 (1992).
12. Arita, K. *et al.* Recognition of modification status on a histone H3 tail by linked histone reader modules of the epigenetic regulator UHRF1. *Proc. Natl Acad. Sci. USA* **109,** 12950–12955 (2012).
13. Hu, L., Li, Z., Wang, P., Lin, Y. & Xu, Y. Crystal structure of PHD domain of UHRF1 and insights into recognition of unmodified histone H3 arginine residue 2. *Cell Res.* **21,** 1374–1378 (2011).
14. Rajakumara, E. *et al.* PHD finger recognition of unmodified histone H3R2 links UHRF1 to regulation of euchromatic gene expression. *Mol. Cell* **43,** 275–284 (2011).
15. Rothbart, S. B. *et al.* Association of UHRF1 with methylated H3K9 directs the maintenance of DNA methylation. *Nature Struct. Mol. Biol.* **19,** 1155–1160 (2012).
16. Nady, N. *et al.* Recognition of multivalent histone states associated with heterochromatin by UHRF1 protein. *J. Biol. Chem.* **286,** 24300–24311 (2011).
17. Song, J., Rechkoblit, O., Bestor, T. H. & Patel, D. J. Structure of DNMT1-DNA complex reveals a role for autoinhibition in maintenance DNA methylation. *Science* **331,** 1036–1040 (2011).
18. Felle, M. *et al.* The USP7/Dnmt1 complex stimulates the DNA methylation activity of Dnmt1 and regulates the stability of UHRF1. *Nucleic Acids Res.* **39,** 8355–8365 (2011).
19. Achour, M. *et al.* The interaction of the SRA domain of ICBP90 with a novel domain of DNMT1 is involved in the regulation of VEGF gene expression. *Oncogene* **27,** 2187–2197 (2008).
20. Lutzmann, M. & Mechali, M. MCM9 binds Cdt1 and is required for the assembly of prereplication complexes. *Mol. Cell* **31,** 190–200 (2008).
21. Citterio, E. *et al.* Np95 is a histone-binding protein endowed with ubiquitin ligase activity. *Mol. Cell. Biol.* **24,** 2526–2535 (2004).
22. Jenkins, Y. *et al.* Critical role of the ubiquitin ligase activity of UHRF1, a nuclear RING finger protein, in tumor cell growth. *Mol. Biol. Cell* **16,** 5621–5629 (2005).
23. Karagianni, P., Amazit, L., Qin, J. & Wong, J. ICBP90, a novel methyl K9 H3 binding protein linking protein ubiquitination with heterochromatin formation. *Mol. Cell. Biol.* **28,** 705–717 (2008).
24. Peng, J. *et al.* A proteomics approach to understanding protein ubiquitination. *Nature Biotechnol.* **21,** 921–926 (2003).
25. Kim, W. *et al.* Systematic and quantitative assessment of the ubiquitin-modified proteome. *Mol. Cell* **44,** 325–340 (2011).
26. Shimamura, S. & Ishikawa, F. Interaction between DNMT1 and DNA replication reactions in the SV40 *in vitro* replication system. *Cancer Sci.* **99,** 1960–1966 (2008).
27. Takebayashi, S., Tamura, T., Matsuoka, C. & Okano, M. Major and essential role for the DNA methylation mark in mouse embryogenesis and stable association of DNMT1 with newly replicated regions. *Mol. Cell. Biol.* **27,** 8243–8258 (2007).
28. Plechanovová, A., Jaffray, E. G., Tatham, M. H., Naismith, J. H. & Hay, R. T. Structure of a RING E3 ligase and ubiquitin-loaded E2 primed for catalysis. *Nature* **489,** 115–120 (2012).
29. Muraki, K., Nabetani, A., Nishiyama, A. & Ishikawa, F. Essential roles of *Xenopus* TRF2 in telomere end protection and replication. *Genes Cells* **16,** 728–739 (2011).
30. Nishiyama, A., Frappier, L. & Mechali, M. MCM-BP regulates unloading of the MCM2–7 helicase in late S phase. *Genes Dev.* **25,** 165–175 (2011).

Supplementary Information is available in the online version of the paper.

Acknowledgements We are grateful to T. S. Takahashi, K. Shintomi, K. Muraki, H. Nakaoka, M. Iwabuchi and K. Ohsumi for reagents and technical advice, J. Maller for *Xenopus* Orc2 antibody, H. Miyoshi for lentiviral vectors, K. Helin for reading of the manuscript and M. Orii for designing the schematic diagram shown in Supplementary Fig. 1. We thank A. Hosoi and C. Yamada-Namikawa for technical assistance. M.N. was supported by a Grant-in-Aid for Scientific Research on Innovative Areas 'Cell fate control', Scientific Research (A), and Challenging Exploratory Research from MEXT Japan. A.N. was supported by a Research Activity Start-up and Grant-in-Aid for Young Scientists (B) from the Japan Society for the Promotion of Science.

Author Contributions M.N. and A.N. planned studies and interpreted the data. A.N. and L.Y. performed most of the *Xenopus* studies. J.S. and H.K validated the *mUhrf1* knockout lines and performed bisulphite DNA sequencing analysis. Y.J. and K.N. performed most of the mammalian studies. T.Kaw. and T.Kod. performed LC–MS/MS analysis. S.S. and F.I. generated purified recombinant mDnmt1 proteins. K.A. generated the purified recombinant hUhrf1 protein. M.N. and A.N wrote the paper.

Author Information Reprints and permissions information is available at www.nature.com/reprints. The authors declare no competing financial interests. Readers are welcome to comment on the online version of the paper. Correspondence and requests for materials should be addressed to M.N. (mkt-naka@med.nagoya-cu.ac.jp) or A.N. (anishiya@med.nagoya-cu.ac.jp).

METHODS

Plasmids and proteins. Full-length xUhrf1 was isolated from *Xenopus* total egg cDNA by PCR. The cDNA fragment of xUhrf1 that encodes amino acids 1–650 was cloned into pET16b to be expressed as His-tagged protein. The expression constructs for His-tagged geminin and GST-tagged p27 were gifts from T. S. Takahashi. His- and GST-tagged fusion proteins were expressed in *Escherichia coli* BL21-CodonPlus-RIL cells (Stratagene), purified using standard molecular biology techniques, and stored in aliquots at −80 °C until use. Recombinant His-tagged ubiquitin and its mutant proteins were purchased from Boston Biochem. rmDnmt1 and its mutant were prepared as described previously[26].

Antibodies. Antibodies against xUhrf1 were raised in rabbits by immunization with a His_{10}-tagged, recombinant peptide (1–650) of xUhrf1. The anti-xDnmt1 antibody was raised against a synthetic peptide (CTETVKAEKMETD). Antisera were further affinity-purified with the recombinant protein immobilized onto a nitrocellulose membrane. Anti-xOrc2 was kindly provided by J. Maller. Anti-xPcna (Sigma, PC10), xUsp7 (Bethyl Laboratories, A300-033A), ubiquitin (Santacruz, P4D1), xMcm7 (Abcam, ab2360), H3 (Abcam, ab1791), hDnmt1 (Santacruz, H300), hUhrf1 (BD Biosciences, 612264), mUhrf1 (Santacruz, M-132), HA (MBL, 561), Myc (Santacruz, A-14), Myc (Santacruz, 9E10), Flag (Sigma, M2), His (MBL, PM032), horseradish-peroxidase-conjugated protein A (GE healthcare, NA9120V), (Santacruz, P4D1) and Pcna (Santacruz, PC10) were obtained commercially.

***Xenopus* egg extracts.** Cytostatic factor (CSF)-arrested and interphase egg extracts were prepared as described[29,30], except that metaphase II-arrested eggs were washed in extraction buffer (EB; 5 mM $MgCl_2$, 100 mM KCl, 20 mM HEPES-KOH, pH 7.5) instead of in 1× Marc's modified Ringers (MMR). Incubations of extracts were carried out at 22 °C. For immunoblotting analysis, extracts were diluted 20-fold with SDS sample buffer and boiled for 5 min.

Immunodepletion. For immunodepletion of *Xenopus* egg extracts, 250 μl of antiserum against xUhrf1 and xDnmt1 were conjugated to 75 μl of protein A agarose (Roche). Twenty-five microlitres of antibody beads were mixed with 100 μl interphase egg extracts and incubated at 4 °C for 1 h. This was repeated three times. For add-back experiments, mDnmt1 wild-type or the C1229S mutant was added to xDnmt1-depleted extracts at 10 ng μl^{-1}.

Monitoring DNA methylation and replication in *Xenopus* egg extracts. DNA methylation was monitored by the incorporation of *S*- [methyl-^{3}H]-adenosyl-L-methionine. Demembranated sperm nuclei (3,000 nuclei per μl) were added to an egg extract containing *S*-[methyl-^{3}H]-adenosyl- L-methionine, incubated at room temperature (22–25 °C), and the reaction was stopped by the addition of chromatin purification buffer (CPB; 50 mM KCl, 5 mM $MgCl_2$, 20 mM HEPES-KOH, pH 7.7, and 2% sucrose) up to 300 μl. His_6–geminin, GST–p27 or aphidicolin (150 μM) was added to the extracts 10 min before the addition of sperm DNA. Genomic DNA was purified using a Wizard Genomic DNA purification kit (Promega) according to the manufacturer's instructions. The DNA replication efficiency was determined as described previously[20].

Isolation of chromatin fractions from *Xenopus* egg extracts. Sperm nuclei were incubated in extracts at a concentration of 3,000 nuclei per μl. Each 30–50-μl extract was diluted fivefold with ice-cold CPB containing 0.1% NP40, overlaid onto a 30% sucrose/CPB cushion, and centrifuged at 15,000*g* for 10 min. The pellets were re-suspended in SDS sample buffer. For MS/MS analysis, to enrich histone proteins, chromatin fractions were washed in 300 mM NaCl and acid-extracted.

Immunoprecipitation. Two micrograms of the antibody for immunoprecipitation were incubated with protein A-agarose beads for 1 h at room temperature and washed in CPB buffer. *Xenopus* egg extracts were diluted fivefold in CPB buffer and incubated with the antibody-bound beads for 1 h at 4 °C. Beads were then washed twice with CPB, once with CPB containing 0.1% Triton X-100, and twice with CPB alone. Proteins were finally eluted with SDS sample buffer and analysed by SDS–PAGE.

Immunoprecipitation of chromatin-bound histone H3. Extracts containing sperm chromatin were diluted fivefold with CPB containing 0.1% NP-40, and were then incubated on ice for 5 min. The chromatin was isolated via centrifugation at 10,000*g* for 10 min through a 0.5-ml sucrose cushion of CPB with 30% sucrose, which was underlayered in the tube with 10 μl of 2 M sucrose. Removal of the supernatant by aspiration left 50 μl and an equal volume of nuclease buffer (micrococcal nuclease) was added. The chromatin pellet was re-suspended by vortexing and incubated at 22 °C for 20 min. The reaction was stopped by the addition of 10 mM EDTA and the tube was centrifuged at 15,000 r.p.m. for 10 min. For H3 immunoprecipitation, the supernatant was supplemented with 1% SDS and was diluted tenfold with lysis buffer (1% Triton X-100, 1 mM EDTA, 150 mM NaCl, 15 mM Tris-HCl, pH 8.0). Diluted lysates were incubated with 2 μg of histone H3 antibody conjugated to 10 μl of protein A agarose. Beads were then washed three times with 400 μl of lysis buffer. For a pulldown experiment, immunoprecipitated histone H3 was incubated with egg extract at 4 °C for 1 h. Beads were washed four times with lysis buffer and bound proteins were finally eluted with SDS sample buffer and analysed by SDS–PAGE.

Pulldown of xUbH3 by immunopurified xDnmt1. Immunoprecipitation of xDnmt1 was performed as described above. Immunopurified xDnmt1 bound to protein A agarose was incubated with 40 μl of the MNase-digested chromatin fraction isolated from either mock- or xDnmt1-depleted extracts. After incubation on ice for 1 h, beads were washed with CPB buffer containing 0.1% NP-40. Bound proteins were analysed by immunoblotting.

Purification of rhUhrf1. A DNA fragment encoding full-length hUhrf1 was amplified by PCR and cloned into pGEX-6P plasmid (GE Healthcare Bio-Sciences). The recombinant protein was overexpressed in the *E. coli* strain Rosetta (DE3). Cells were grown at 37 °C in Luria-Bertani medium, induced with 0.1 mM isopropyl-β-D-thiogalactopyranoside (IPTG) when they reached an optical density of 0.5∼0.6 at 660 nm and were then incubated at 15 °C overnight.

The cells were collected, re-suspended in lysis buffer (50 mM Tris-HCl, pH 8.0, containing 300 mM NaCl, 1 mM dithiothreitol (DTT), 30 μM ZnOAc, 10% glycerol and 0.2 mM phenylmethylsulphonyl fluoride (PMSF)) and disrupted by sonication on ice. After centrifugation, the supernatant was applied to a GST affinity column of glutathione Sepharose 4 Fast Flow (GE Healthcare Bio-Sciences) equilibrated with PMSF-free lysis buffer and eluted by digestion using PreScisson protease. The protein was further purified by anion-exchange chromatography using a HiTrap Q HP column, by DNA binding protein affinity chromatography using a HiTrap Heparin column and by size-exclusion chromatography using a HiLoad 26/60 Superdex200 column (GE Healthcare Bio-Science).

Trypsin digestion and LC–MS/MS. The method for trypsin digestion of protein has been described previously[31]. LC–MS/MS analysis was performed using an LTQ orbitrap ELITE ETD mass spectrometer (Thermo Fisher Scientific). The methods used for LC–MS/MS were slightly modified from those described previously[32]. The mass spectrometer was operated in data-dependent acquisition mode in which MS acquisition with a mass range of m/z 350–1,600 was automatically switched to MS/MS acquisition under the control of Xcalibur software. The top three precursor ions in the MS scan were selected by Orbitrap, with a resolution of R = 240,000, and those in subsequent MS/MS scans, with an ion trap in automated gain control (AGC) mode where AGC values were 1×10^6 and 1.00×10^4 for full MS and MS/MS, respectively. For fragmentation, collision-induced dissociation and electron transfer dissociation were used.

Database searching. Tandem mass (MS/MS) spectra were extracted using Proteome Discoverer version 1.3. All MS/MS samples were analysed using Mascot (Matrix Science; version 2.4). Mascot was set up to search Sprot_2012_08.fasta (selected for *Xenopus laevis*, 3,350 entries) assuming the presence of the digestion enzyme trypsin. Mascot was searched with a fragment ion mass tolerance of 0.80 Da and a parent ion tolerance of 3.0 p.p.m. The maximum number of missed cleavage sites was set at 3. The carbamidomethyl of cysteine was specified in Mascot as a fixed modification. Amide of arginine, methyls of lysine and arginine, dimethyls of lysine and arginine, acetyl of lysine, trimethyl of lysine, phosphos of serine, threonine and tyrosine, GlyGly of lysine and LeuArgGlyGly of lysine, all of which have a trypsin-digested ubiquitinated protein signature, were specified in Mascot as variable modifications[24].

Criteria for protein identification. Scaffold (version Scaffold_3.6.3, Proteome Software) was used to validate MS/MS-based peptide and protein identifications. Peptide identifications were accepted if they could be established at greater than 95.0% probability as specified by the Peptide Prophet algorithm[33]. Protein identifications were accepted if they could be established at greater than 99.0% probability and contained at least three identifiable peptides. Protein probabilities were assigned by the Protein Prophet algorithm[34]. Proteins that contained similar peptides and could not be differentiated based on MS/MS analysis alone were grouped together to satisfy the principle of parsimony.

Plasmid construction. To generate lentivirus-based *sh-hDnmt1* or *sh-hUhrf1* constructs, an oligonucleotide containing the nucleotides 303–321 of *hDnmt1* (forward 5′- GATCCCC**GGAGGTGAATGGATGTCTA**ACGTGTGCTGTCC GT**TAGACGTCCATTCACTTCC**TTTTTGGAAAT-3′ and reverse 5′- CTAGA TTTCCAAAAA**GGAAGTGAATGGACGTCTA**ACGGACAGCACACGT**TAG ACATCCACTCACCTCC**GGG-3′; targeting sequence in bold) or nucleotides 1486–1505 of *hUhrf1* (forward 5′-GATCCCC**GGTCGATGGGTACGTTGAT**A CGTGTGCTGTCCGT**ATCGACGTACTCATTGACC**TTTTTGGAAAT-3′ and reverse 5′-CTAGATTTCCAAAAA**GGTCAATGAGTACGTCGAT**ACGGACA GCACACGT**ATCAACGTACCCATCGACC**GGG-3′; targeting sequence in bold) was annealed and inserted into pENTR4-H1 (a gift from H. Miyoshi) digested with AgeI/EcoRI. To insert the H1tetOx1-shRNA into a lentivirus vector, we mixed the resulting pENTR4-H1-shRNA vector and CS-RfA-ETBsd (a gift from H. Miyoshi) or CS-RfA-ETHygro vector with Gateway LR clonase (Invitrogen).

To construct the plasmid, pCAGGS-hH3-Flag, the BamHI (end-filled)/EcoRI (end-filled) fragment containing the full-length cDNA and the Flag epitope from a

pOZ-C-hH3 (a gift of H. Tagami, Nagoya City University) was inserted into a pCAGGS vector digested with EcoRI (end-filled). The hH3(K23R) mutant plasmid was generated by PCR-based, site-directed mutagenesis for pCAGGS-hH3-Flag. To construct pCAG-puro-Myc-mUhrf1, a PCR fragment containing the full-length cDNA was sub-cloned into pCAG-puro-Myc vector. The pCAG-pruo-Myc-mUhrf1 mutant plasmids were generated by PCR-based, site-directed mutagenesis for pCAG-puro-Myc-mUhrf1.

Immunoprecipitation and immunoblotting analyses for mammalian cells. 293T cells or HeLa cells transfected with the indicated constructs were lysed as quickly as possible in TBSN buffer (20 mM Tris-Cl, pH 8.0, 150 mM NaCl, 0.5% NP-40, 5 mM EGTA, 1.5 mM EDTA, 0.5 mM Na3VO4, 50 μM PR-619 and 20 mM *p*-nitrophenylphosphate (PNPP). The resulting lysates were clarified by centrifugation at 15,000*g* for 20 min at 4 °C before immunoprecipitation with the specified antibody. Immunoprecipitated proteins were separated by SDS–PAGE, transferred to a polyvinylidene difluoride (*Immobilon*-P; Millipore) membrane and then detected by immunoblotting with the indicated antibodies using an enhanced chemiluminescence detection system.

Denaturing Immunoprecipitation. Denaturing immunoprecipitation was performed according to the Abcam protocol with a slight modification. In brief, HeLa cells were lysed in denaturing buffer (50 mM Tris-Cl, pH 8.0, 1% SDS, 5 mM EDTA, 10 mM DTT, 15 U ml^{-1} DNaseI, 50 μM PR-619 and protease inhibitors), and the lysates were heated at 95 °C for 10 min and clarified by centrifugation at 15,000*g* for 5 min at 20 °C. The supernatant was diluted ten times with non-denaturing buffer (50 mM Tris-Cl, pH 8.0, 250 mM NaCl, 10% glycerol, 1% NP-40, 5 mM EDTA, 50 μM PR-619 and protease inhibitors), and the lysates were used for immunoprecipitation with Flag M2 agarose. The immunoprecipitates were washed four times with non-denaturing buffer, and used for the binding assay with rmDnmt1 protein.

Cell culture, transfection and virus generation and infection. Cell lines were cultured as recommended by American Type Culture Collection (Manassas). HeLa cells were trapped in S phase by treating them with 2.5 mM thymidine (Sigma) for 20 h. Transfection was routinely carried out with lipofectamine 2000 (Invitrogen). For the production of lentiviruses, transfection was performed by the calcium phosphate co-precipitation method[35]. Lentiviruses expressing shRNA were generated by co-transfecting 293T cells with pCMV-VSV-G-RSV-RevB (a gift from H. Miyoshi), pCAG-HIVgp (a gift of H. Miyoshi), and the respective CS-RfA-ETBsd or CS-RfA-ETHygro vector. HeLa cells infected with the viruses were treated with 10 μg ml^{-1} blasticidin (Invitrogen) and/or 200 ng ml^{-1} hygromycin (Sigma) for 2–3 days. To generate mUhrf1-expressing cells, PvuI-linearized pCAG-puro-Myc-mUhrf1 plasmids were cut with PvuI and transfected into the cells by the calcium phosphate co-precipitation method. Cells transfected with the indicated plasmids were treated with 2 μg ml^{-1} of puromycin (Sigma) for 5 days.

Histone acid extraction. Cell pellets were re-suspended in PBS with 0.5% Triton X-100 and protease inhibitors at a density of approximately 10^7 cells ml^{-1} and tubes were rotated at 4 °C for 10 min to lyse the cells. The lysates were centrifuged at 4 °C for 10 min at 2,000 r.p.m., and the pellets were rinsed once in the extraction buffer. The histones in the insoluble chromatin pellet were then extracted in 0.2 N HCl for 10 min at 4 °C on a rotator. The lysates were centrifuged at 4 °C for 10 min at 2,000 r.p.m., and the supernatants containing histones were collected and adjusted to pH 8.0 with 2 M Tris.

Immunofluorescence analysis. Mouse embryonic fibroblasts grown onto glass slides were treated with 0.1% Triton X-100 in CSK buffer (100 mM NaCl, 300 mM sucrose,10 mM PIPES, pH 6.8, 3 mM $MgCl_2$ and 1 mM EGTA) for 2 min at 4 °C, fixed with 4% paraformaldehyde in PBS, and then treated with methanol for 20 min at −20 °C. The cells were incubated in blocking solution (5% BSA in PBS) and incubated in detection solution containing primary antibodies (5% BSA in PBS). After four washes with PBS, the samples were incubated in detection solution containing the secondary antibodies. Images were collected using BZ-9000 (KEYENCE).

Matintenance of *Uhrf*$^{fl/fl}$ embryonic stem cells. *Uhrf*$^{fl/fl}$ embryonic stem cells were cultured on mitomycin-C-treated non-proliferating feeder mouse embryonic fibroblast cells in standard embryonic stem cell medium supplemented with 20% FBS and LIF. For conditional knockout of the endogenous *mUhrf1* gene, 800 nM 4-OH tamoxifen (4-OHT, SIGMA, no. H7904, dissolved in ethanol) was added to the medium. Ablation of the *mUhrf1* transcript was confirmed by qPCR using the following primers specific for *mUhrf1* exons 4 and 5, mUhrf1-RT-F01, ATG ATTGCAGAGGGGAGTTG; and mUhrf1-RT-R01, GTGGTGAGGGGAGTGA AGAA. Decreases in mUhrf1 protein expression were assessed using an Uhrf1-specific antibody (Uhrf1, M-132 antibody, Santa Cruz Biotechnology, no. sc-98817). Expression of the Myc-tagged exogenous wild-type or mutant Uhrf1 proteins was detected with a mouse monoclonal anti-Myc tag antibody (Millipore, 05-724, clone 4A6).

Wild-type and mutant Uhrf1-expressing mouse embryonic stem cell cloning. Six micrograms of linearized pCAG-IRES-Puro plasmid containing either a Myc-tagged wild-type, an SRA domain mutant (D474A/R489A) or a RING domain mutant (C713A/C715A/C716A) *mUhrf1* cDNA were transfected into *Uhrf1*$^{fl/fl}$ embryonic stem cells using FuGENE HD transfection reagent (Roche Applied Science, no. 6366244). Stable clones were selected by puromycin (1 mg ml^{-1}) treatment. Endogenous *mUhrf1* genes are conditionally deleted by the addition of 4-hydroxytamoxifen from *Uhrf1*$^{fl/fl}$ embryonic stem cells expressing ER-Cre.

Global DNA methylation analysis by methylation-sensitive Southern blotting. Endogenous *mUhrf1* genes were conditionally deleted by the addition of 4-hydroxytamoxifen from *Uhrf1*$^{fl/fl}$ embryonic stem cells expressing ER-Cre. Genomic DNA was purified from embryonic stem cells using an AllPrep DNA/RNA mini kit (QIAGEN, no. 80204) according to the supplier's protocol. One microgram of genomic DNA was treated with 20 U HpaII (New England BioLabs, no. R0171L) or 10 U MspI (New England BioLabs, no. R0106L) overnight at 37 °C. Digests were separated with 0.8% agarose-gel, transferred to a nylon membrane and hybridized with specific probes generated with the following primers: 5′-AGTGGGCAGA GTATTCTCTG-3′; IAP-LTR-probeF, 5′-CAGAAGATTCTGGTCTGTGGTGTT-3′; IAP_LTR_probeR, 5′-GAATTCATACAGTTGAATCCTTCT-3′; MLV_gag_probeF, 5′-TCGAGATCATGGGACAGACC-3′; and MLV_gag_probeR, GGGTAAGGG CAGGGTAAAGG-3′. Relative DNA methylation was determined by counting radioactivity of the undigested DNA (tops of the gels) and represented as a percentage of DNA undigested by HpaII in *Uhrf1*$^{fl/fl}$ mouse embryonic stem cells.

Bisulphite DNA sequencing analysis. Two micrograms of genomic DNA were treated with sodium bisulphite using an EpiTect bisulphite kit (QIAGEN, no. 59104) following the manufacturer's protocol. The Gag region of the IAP retrotransposons was amplified from the bisulphite-treated genomic DNA using the following primers: IAP-Gag-BS-F01, 5′-ATTTTGTTGATTAAATAAATTATTA TTGGG-3′; and IAP-Gag-BS-R01, 5′-TAAAACATATCCTCTAATCATTTCT ACTCA-3′. Primers for minor satellites: forward, 5′-ATTATATTGTAGAATA TATTAGATGAGTGAG-3′; reverse, 5′-ATCATTTTCCATATTTCTCATTAT AACTC-3′. PCR products were cloned into TOPO TA Cloning Dual Promoter vector (Life Technologies, no. K4600-01). Successful clones were sequenced using a BigDye Terminator v3.1 Cycle Sequencing kit (Applied Biosystems, no. 4337454). Methylated CpGs are shown as closed circles and unmethylated ones are represented with open circles.

***In vitro* deubiquitylation assays.** For the substrate, hUbH3 was acid-extracted from hDnmt1-depleted HeLa cells which were released 4 h from the G1/S boundary by double thymidine treatment. The hUbH3 was mixed with immune-precipitated xDnmt1 from *Xenopus* egg extract in reaction buffer (50 mM Tris-HCl, pH 7.5, 150 mM NaCl, 2 mM EDTA, 2 mM DTT) for 8 h at 37 °C. To block the reactions, Laemmli buffer was added to the reaction, and the proteins were analysed by immunoblotting.

31. Fujinoki, M. *et al.* Identification of 36-kDa flagellar phosphoproteins associated with hamster sperm motility. *J. Biochem.* **133,** 361–369 (2003).
32. Daigo, K. *et al.* The proteomic profile of circulating pentraxin 3 (PTX3) complex in sepsis demonstrates the interaction with azurocidin 1 and other components of neutrophil extracellular traps. *Mol. Cell. Proteomics* **11,** M111.015073 (2012).
33. Keller, A., Nesvizhskii, A. I., Kolker, E. & Aebersold, R. Empirical statistical model to estimate the accuracy of peptide identifications made by MS/MS and database search. *Anal. Chem.* **74,** 5383–5392 (2002).
34. Nesvizhskii, A. I., Keller, A., Kolker, E. & Aebersold, R. A statistical model for identifying proteins by tandem mass spectrometry. *Anal. Chem.* **75,** 4646–4658 (2003).
35. Chen, C. & Okayama, H. High-efficiency transformation of mammaiian cells by plasmid DNA. *Mol. Cell. Biol.* **7,** 2745–2752 (1987).

frontiers in ONCOLOGY

REVIEW ARTICLE
published: 31 January 2013
doi: 10.3389/fonc.2013.00008

Response to DNA damage: why do we need to focus on protein phosphatases?

Midori Shimada* and Makoto Nakanishi*

Department of Cell Biology, Graduate School of Medical Sciences, Nagoya City University, Nagoya, Japan

Edited by:
Mira Jung, Georgetown University, USA

Reviewed by:
Fatih Uckun, University of Southern California, USA
Zhenkun Lou, Mayo Clinic, USA

****Correspondence:***
Midori Shimada and Makoto Nakanishi, Department of Cell Biology, Graduate School of Medical Sciences, Nagoya City University, 1-Kawasumi, Mizuho-cho, Mizuho-ku, Nagoya 467-8601, Japan.
e-mail: midorism@med.nagoya-cu.ac.jp; mkt-naka@med.nagoya-cu.ac.jp

Eukaryotic cells are continuously threatened by unavoidable errors during normal DNA replication or various sources of genotoxic stresses that cause DNA damage or stalled replication. To maintain genomic integrity, cells have developed a coordinated signaling network, known as the DNA damage response (DDR). Following DNA damage, sensor molecules detect the presence of DNA damage and transmit signals to downstream transducer molecules. This in turn conveys the signals to numerous effectors, which initiate a large number of specific biological responses, including transient cell cycle arrest mediated by checkpoints, DNA repair, and apoptosis. It is recently becoming clear that dephosphorylation events are involved in keeping DDR factors inactive during normal cell growth. Moreover, dephosphorylation is required to shut off checkpoint arrest following DNA damage and has been implicated in the activation of the DDR. Spatial and temporal regulation of phosphorylation events is essential for the DDR, and fine-tuning of phosphorylation is partly mediated by protein phosphatases. While the role of kinases in the DDR has been well documented, the complex roles of protein dephosphorylation have only recently begun to be investigated. Therefore, it is important to focus on the role of phosphatases and to determine how their activity is regulated upon DNA damage. In this work, we summarize current knowledge on the involvement of serine/threonine phosphatases, especially the protein phosphatase 1, protein phosphatase 2A, and protein phosphatase Mg^{2+}/Mn^{2+}-dependent families, in the DDR.

Keywords: DNA damage response, phosphorylation, protein phosphatase, DNA repair, chromatin

INTRODUCTION

The DNA damage response (DDR) signaling network mediates a wide variety of cellular events, including DNA repair, cell cycle arrest, apoptosis, and premature senescence, to maintain genomic integrity. Loss of checkpoint function results in chromosomal instability and aneuploidy, which promote tumorigenesis, suggesting that proper checkpoint signaling is essential for preventing cancer. From recent studies, it has become clear that protein phosphorylation plays a major role in the regulation of diverse DDR pathways. The initiation of some DDR processes is mainly mediated by protein kinases in the phosphoinositide 3-kinase (PI3-K)-related kinase family, as well as ataxia-telangiectasia mutated (ATM), ATM and Rad3-related (ATR), and DNA-dependent protein kinase (DNA-PK). These kinases orchestrate the cellular responses to DNA damage and activate the multiple cascades involved in the DDR through phosphorylation of a variety of substrates (Shiloh, 2003). Effector kinases, Chk1 and Chk2, are activated mainly by ATR and ATM, respectively, and transmit signals to a variety of downstream factors, such as p53, pRB, and Cdc25, ultimately leading to inactivation of cyclin-dependent kinases (Cdks) and inhibiting cell-cycle progression. Thus, studies have demonstrated that protein phosphorylation, mainly at serine (S)/threonine (T) residues, is essential for the DDR and regulates enzymatic activity, localization, protein–protein interactions, and stabilization. Given the fact that ATM and ATR are known to have hundreds of substrates, a large number of phosphorylation events are regulated and have roles in the DDR, although the biological significance of many of these phosphorylation events is largely unknown. Indeed, the catalytic subunits of protein phosphatases and their regulators are also targets of ATM and ATR, suggesting that the activity of protein phosphatases is regulated by phosphorylation during the DDR.

Recent large proteomic analyses have revealed that most phosphorylation events are tightly regulated both spatially and temporally, suggesting that a comprehensive analysis of the timing and location of phosphorylation events, rather than analysis of phosphorylation levels in whole cells, is essential to understand the DDR. In recent years, it has become increasingly clear that phosphatases, particularly S/T phosphatases, regulate the DDR not only by counteracting the function of kinases, but also by initiation of specific steps during the DDR. Given that fine-tuning of phosphorylation events is partly mediated by phosphatases, studies should focus on the involvement of protein phosphatases in the DDR and how their activity is regulated *in vivo*. In addition to phosphorylation, different types of post-translational modifications also have important roles in the DDR. Thus, it will be important to investigate the correlation between phosphorylation/dephosphorylation and other types of modifications. In this study, we summarize recent reports that have revealed new functions of S/T phosphatases in the DDR.

INTRODUCTION TO THE DDR

Upon formation of DNA double-strand breaks (DSBs), ATM is autophosphorylated at S1981 and then dissociates from an inactive homodimer into active monomers (Bakkenist and Kastan, 2003). It has been reported that phosphorylation of ATM on S367, S1893, and S1981 is required for ATM activation in human cells (Bakkenist and Kastan, 2003; Kozlov et al., 2006). Contrary to these findings, corresponding phosphorylation of these sites are dispensable for murine ATM activation (Pellegrini et al., 2006; Daniel et al., 2008). Instead of ATM activation, S1981 phosphorylation is required for ATM retention at sites of DSBs through interaction with mediator of DNA damage checkpoint 1 (MDC1; So et al., 2009). ATM is recruited to DSBs and activated by the MRN complex (Mre11, Rad50, and NBS1) through the association with NBS1 (Uziel et al., 2003; Falck et al., 2005; Lee and Paull, 2005). In response to DSBs, ATM phosphorylates histone H2AX at S139 (termed γ-H2AX), which extends up to megabases away from break sites that are readily visible as foci by immunofluorescence microscopy (Burma et al., 2001; Ward and Chen, 2001; Shroff et al., 2004; Stiff et al., 2004). These γ-H2AX foci are colocalized with many proteins involved in the DDR, such as MDC1, 53BP1, BRCA1, and the MRN complex (Paull et al., 2000). Indeed, γ-H2AX is required for the recruitment and maintenance of these factors at damaged sites in order to transmit signals to downstream factors.

Following single-stranded DNA (ssDNA) damage, replication defects, or during the process of DSBs, ATR, which forms a complex with ATRIP, is recruited to the region of replication protein A (RPA)-coated ssDNA (Zou and Elledge, 2003). Rad17, associated with small subunits of replication factor C (RFC), recognizes the junctions between ssDNA and dsDNA and facilitates the loading of the Rad9-Rad1-Hus1 (9-1-1 complex) sliding clamp onto the DNA (Kondo et al., 2001; Melo et al., 2001; Zou and Elledge, 2003). In concert with ATR/ATRIP and RPA, the 9-1-1 complex appears to act as a sensor of DNA damage and interacts with TopBP1, thereby loading it onto sites of DNA damage. Rad17 interacts with Claspin to promote the phosphorylation of Chk1 (Roos-Mattjus et al., 2002; Bermudez et al., 2003; Wang et al., 2006). All of these proteins, i.e., ATRIP, RPA, RAD17, the 9-1-1 complex, and TopBP1, are phosphorylated by ATR during checkpoint activation. Through an interaction with TopBP1, ATR becomes fully active, thereby inducing subsequent responses (Delacroix et al., 2007; Lee et al., 2007a).

ATR and ATM phosphorylate and activate the effector kinases Chk1 and Chk2, respectively. Chk1 is composed of N-terminal catalytic domain and a regulatory C-terminus, which negatively regulates Chk1 kinase activity. Several reports have identified the functional roles of Chk1 phosphorylation *in vivo*. In response to cellular stresses, Chk1 phosphorylation occurs primarily on 2 residues, S317 and S345 (Liu et al., 2000; Zhao and Piwnica-Worms, 2001). Phosphorylated Chk1 is released from chromatin and accumulates in the cytoplasm to prevent activation of Cdk1 and entry into mitosis (Kramer et al., 2004). Phosphorylation of the C-terminal residues (mainly S317 and S345) block intramolecular interactions, reversing this autoinhibition mechanism (Katsuragi and Sagata, 2004). Regardless of this negative regulatory mechanism, Chk1 has basal activity in its unmodified form, and this activity is sufficient to phosphorylate several substrates, including histone H3 at T11 and Aurora B (Falck et al., 2005; Shimada et al., 2008). Thus, phosphorylation of S317 and S345 induces conformational changes that permit full activation and spatiotemporal regulation of Chk1 (Katsuragi and Sagata, 2004; Ng et al., 2004; Clarke and Clarke, 2005; Smits et al., 2006; Loffler et al., 2007; Niida et al., 2007). Upon DSBs, Chk2 is phosphorylated at T68 by ATM, which triggers Chk2 dimerization and activation by autophosphorylation of residues T383 and T387 in the T-loop (Ahn et al., 2000; Melchionna et al., 2000; Xu et al., 2002). Given that chromatin-bound Chk2 is dissociated from chromatin in response to ionizing radiation (IR), this notion also suggests that Chk2, when localized other than undamaged sites, may allow further activation of downstream effectors (Li and Stern, 2005). Although biochemical analyses revealed that Chk2 can phosphorylate Cdc25A, Cdc25C, BRCA1, and p53, examination of Chk2-deficient mice and cells showed that Chk2 functions mainly in p53-dependent apoptosis (Jack et al., 2002). It is noteworthy that Chk2 and Chk1 have partially redundant roles and share multiple substrates (Bartek and Lukas, 2003; Uziel et al., 2003; Lee and Paull, 2005). However, despite their overlapping roles in checkpoint signaling, the biological requirements for Chk1 and Chk2 function are strikingly different (Bartek and Lukas, 2003). In any case, these checkpoint kinases phosphorylate effector molecules, such as p53 and Cdc25 proteins, to induce cell cycle arrest (Sanchez et al., 1997; Hirao et al., 2000; Shieh et al., 2000; Falck et al., 2001).

DNA-dependent protein kinase plays a critical role in DNA damage repair, especially in non-homologous end-joining (NHEJ) repair of DSBs. DNA-PK is composed of three factors, a catalytic subunit (DNA-PKcs), Ku70, and Ku80, the latter two of which form a Ku heterodimer, and is essential for NHEJ to repair DNA DSBs. The Ku70/Ku80 heterodimer first binds to each broken DNA strand, after which DNA-PKcs is recruited to the DNA ends through interaction with the Ku heterodimer (Gottlieb and Jackson, 1993), promoting DNA repair. Importantly, DNA-PKcs is autophosphorylated at multiple sites and the regions of 2023–2056 and 2609–2647 are identified as major autophosphorylation clusters (Ding et al., 2003; Block et al., 2004; Chen et al., 2005; Cui et al., 2005). Among them, S2056 and T2609 are phosphorylated following IR and extensively studied. Such autophosphorylation of DNA-PKcs is important for end processing, disassembly, and inactivation (Merkle et al., 2002). Functional analysis using hypo- or hyperphosphorylated mutations of DNA-PKcs suggest that timely phosphorylation and dephosphorylation are essential for its function (Chan et al., 2002).

DYNAMIC CHANGES IN PROTEIN PHOSPHORYLATION FOLLOWING DNA DAMAGE

Protein phosphorylation is one of the most common post-translational modifications and is known to control many cellular processes. The phosphorylation state of a protein represents a balance between the activity of protein kinases and protein phosphatases. It has been reported that one-third of cellular proteins are phosphorylated, and more than 98% of protein phosphorylation

occurs on S and T residues (Olsen et al., 2006). Recently, several large-scale proteomic studies have revealed that ATM and ATR phosphorylate hundreds of proteins, which are involved in proliferation, cell structure, transcription, metabolic signaling, and RNA splicing (Matsuoka et al., 2007; Smolka et al., 2007; Stokes et al., 2007; Virshup and Shenolikar, 2009). Thus, ATM and ATR coordinate a much wider variety of cellular activities than initially expected. Protein phosphatase catalytic subunits and a number of their regulators were identified by these screens, suggesting that they play a role in the DDR downstream of ATM/ATR, although the functional meaning of these phosphorylation events has not been investigated. Large phosphoproteomic analyses performed in later studies reported dynamic and temporal aspects of phosphorylation and dephosphorylation following DSBs (Bennetzen et al., 2010; Bensimon et al., 2010). Bennetzen et al. (2010) classified the temporal profiles of nearly 600 regulated phosphorylation sites on 209 proteins and revealed that sites phosphorylated shortly after DSBs are enriched in SQ motifs, which are targets of ATM/ATR/DNA-PK, and in novel SXXQ motifs. Importantly, they identified a considerable number of sites that are dephosphorylated immediately after DNA damage. Bensimon et al. (2010) also performed quantitative phosphoproteomics and showed that 40% of DSB-induced phosphorylation events are ATM-independent. In addition, among ATM-dependent phosphorylation events, 75% are not located in SQ/TQ motifs, indicating the involvement of additional kinases activated by ATM. Similar to the results described by Bennetzen et al. (2010), Bensimon et al. (2010) found that more than 300 sites are dephosphorylated following DSBs among approximately 750 regulated phosphorylation sites on nearly 400 proteins; however, the functions of most of these dephosphorylation events have not yet been identified. Protein phosphatases contribute to shutting off DSB-induced phosphorylation during the late DDR; thus, these proteomic analyses suggested an additional function of phosphatases, which play a primary role in initiating some DDR processes.

PROTEIN PHOSPHATASES

The mammalian genome encodes nearly 500 protein kinases, 400 of which are S/T kinases. In contrast, the number of protein phosphatase catalytic subunits (e.g., catalytic subunit of PP1 is referred as PP1C) has been estimated to be 147, of which only about 40 are S/T phosphatases (Moorhead et al., 2007). The fact that so few S/T phosphatases counteract hundreds of distinct S/T kinases can be explained by the ability of phosphatases to form distinct components *in vivo*. Based on sequence, structure, and biological properties, S/T phosphatases can be classified into Mg^{2+}/Mn^{2+}-dependent phosphatases (PPMs) and the more diverse phosphoprotein phosphatases (PPPs). Among the PPP family, PP1 and PP2A are the most abundant isoforms, and their substrates have been relatively well characterized. PP1 and PP2A catalytic subunits interact with a vast number of regulators that target them to specific locations, mediate substrate specificity, and fine-tune phosphatase activity. In fact, mammalian cells contain more than 600 distinct PP1 complexes and approximately 70 PP2A holoenzymes (Ding et al., 2003).

PP1

PP1 catalyzes the majority of protein dephosphorylation events that regulate diverse cellular processes, such as neuronal signaling, muscle contraction, glycogen synthesis, and cell proliferation. Mammals have three PP1 catalytic genes, PP1α, -γ, and -δ, which encode very closely related proteins showing more than 85% similarity, with minor differences primarily at their NH_2 and COOH termini (Cohen, 2002). PP1γ has 2 isoforms, γ1 and γ2, generated by differential splicing of PP1γ. PP1 isoforms are expressed in all tissues and are widely distributed, except for PP1γ2, which is found only in the testes (Shima et al., 1993). PP1 isoforms show distinct subcellular localization, suggesting distinct roles and substrates for these enzymes (Andreassen et al., 1998). However, only a few reports have demonstrated specific differences for PP1 isoforms, since they do not show strict substrate specificities *in vitro* and have overlapping functions in most cases. Specificity is provided to PP1C through association with a large number of regulatory subunits that target catalytic subunits to specific subcellular localization, modulate their activity, and determine substrate specificity. Importantly many proteins involved in the DDR, including BRCA1, pRB, 53BP1, and Cdc25, harbor a PP1c-binding motif, RVxF (Ding et al., 2003; Kuntziger et al., 2011), and are targets of PP1.

The activity of PP1 is regulated by regulatory subunits such as protein phosphatase 1 nuclear targeting subunit (PNUTS), nuclear inhibitor of protein phosphatase 1 (NIPP1), inhibitor 2 (I2), and recruits PP1 onto mitotic chromatin at anaphase (Repo-Man). Most forms of regulation are also achieved through the regulatory subunits; however, phosphorylation of PP1 by Cdk is also important for its activity. Nuclear PP1 shows higher activity in G_0/G_1 and G_2/M, and this change can be explained by Cdk-dependent phosphorylation of PP1 in its C-terminus. Cdk phosphorylates PP1α on T320, reducing its activity (Dohadwala et al., 1994; Berndt et al., 1997; Kwon et al., 1997). The equivalent T residue is conserved in all three PP1 isoforms (T316 in PP1β and T311 in PP1γ), and indeed, PP1γ is also inactivated by Cdk-dependent T311 phosphorylation (Shimada et al., 2010). Mice with depleted PP1γ are viable, but males show defective spermiogenesis and are infertile (Varmuza et al., 1999). These findings suggest that PP1α and/or -β could compensate for the depletion of PP1γ in development, but not in the specific function of spermiogenesis.

THE PP2A FAMILY

PP2 is further divided into three groups on the basis of metal-dependence: metal-independent PP2A, PP4, PP5, and PP6; Ca^{2+}-dependent PP2B and PP7; and Mg^{2+}/Mn^{2+}-dependent PP2C. Among the metal-independent group members, PP4 and PP6 share high homology with PP2A and are referred as PP2A-like phosphatases. Recent reports revealed that PP2A-like phosphatases have overlapping substrates and roles in the DDR.

PP2A

PP2A often functions as a heterotrimer, comprising three subunits designated A, B, and C. The core enzyme consists of the catalytic C subunit, scaffold A subunit, and variable regulatory B subunit. The regulatory B subunit defines the substrate specificity of the

PP2A holoenzyme and comprises four families: PR55/B (B55), PR61/ B′ (B56), PR72/B″, and striatins/SG2NA/B‴. Each one of these families contains various isoforms, which, when combined with the isoforms of both A and C subunits, produce a variety of PP2A holoenzymes that perform distinct functions. Depletion or inhibition of PP2A activity in *Xenopus* egg extracts inhibits the initiation of DNA replication by preventing binding of the initiation factor Cdc45 onto prereplication complexes (Lin et al., 1998; Chou et al., 2002). Additionally, recent studies have uncovered important roles for PP2A in the DDR. For example, PP2A is essential for the activation of ATM, ATR, Chk1, Chk2, and p53 and mediates G_2/M checkpoint control through regulation of the phosphorylation states of these proteins, although phosphorylation of Chk2 at T68, ATR at S428, and Chk1 at S317 is observed even in irradiated cells lacking PP2A activity (Yan et al., 2010).

PP4

PP4 is structurally and functionally related to PP2A and shares 65% amino acid identity with PP2A. PP4c associates with the regulatory subunits PP4R1, PP4R2, PP4R3α, PP4R3β, and PP4R4 (Cohen et al., 2005; Chen et al., 2008). Recent reports have demonstrated that PP4 possesses various cellular functions, including roles in nucleation, growth, and stabilization of microtubules at centrosomes/spindle bodies during cell division (Brewis et al., 1993; Helps et al., 1998; Hastie et al., 2000; Sumiyoshi et al., 2002). PP4 is localized predominantly to the nucleus, but some PP4 is present in cytoplasm and in mitotic centrosomes. Importantly, depletion of PP4 leads to embryonic lethality in mice, and PP4 deficiency in thymocytes results in decreased proliferation, indicating the essential role of PP4 in development and cell growth (Shui et al., 2007). Thanks to the functional analysis of newly identified PP4 substrates, our understanding of the role of PP4 in the DDR has also grown. Indeed, PP4 is involved in recovery from the G2/M checkpoint arrest after IR and required for cell survival in the presence of DNA replication inhibitors (Chowdhury et al., 2008; Nakada et al., 2008).

PP5

Unlike other related phosphatases, PP5 contains tetratricopeptide repeat (TPR) domains at the N-terminus. A catalytic domain and an auto-inhibitory domain are located at the C-terminus (Chinkers, 2001). Moreover, unlike other related phosphatases, whose substrate specificity is mediated by regulatory subunits, PP5 is regulated by protein–protein interactions through the TPR motif. Thus far, PP5 has been reported to interact with several proteins involved in the regulation of steroid signaling (Chen et al., 1996; Silverstein et al., 1997), cell cycle progression (Ollendorff and Donoghue, 1997; Zuo et al., 1998), and apoptosis (Morita et al., 2001) via the TPR domain. In addition, PP5 has been reported to be less abundant than other phosphatases, and has been shown to have low basal activity (Chinkers, 2001). PP5 knockout mice are viable, and the replication checkpoint is intact; however, the G_2/M checkpoint is impaired in PP5-knockout mouse embryonic fibroblasts (MEFs), indicating the essential function of PP5 in the DDR as general regulator of ATM, ATR, DNA-PK, or their substrates, as discussed below (Yong et al., 2007).

PP6

PP6 forms stable heterotrimers, comprising the PP6 catalytic subunit (PP6c), one of the three regulatory subunits (PP6R1, PP6R2, or PP6R3), and one of the three ankyrin repeat-containing subunits (ARS-A, ARS-B, or ARS-C; Stefansson and Brautigan, 2006; Stefansson et al., 2008). Functional analysis of PP6 showed that PP6 regulates G_1 to S progression through controlling cyclin D1 protein expression (Stefansson and Brautigan, 2007) and mitotic spindle formation through inhibition of an essential mitotic kinase, Aurora A (Zeng et al., 2010). Knockdown of either PP6R1 or PP6c impairs DNA-PK activation, DSB repair, and IR sensitivity, indicating that PP6 has critical roles in the DDR (Mi et al., 2009b; Douglas et al., 2010; Zhong et al., 2011).

PP2C

Wip1/PPM1D

PP2C belongs to the Mn^{2+}/Mg^{2+}-dependent PPM family. Unlike the PPP family, PP2C phosphatases are insensitive to inhibition by okadaic acid (OA) or microcystin and do not have regulatory subunits, but instead contain specific regulatory and targeting domains. Among the PP2C phosphatases, wild-type p53-inducible phosphatase 1 (Wip1), also termed PPM1D, which was originally identified in a screen for p53 target genes (Fiscella et al., 1997), has been extensively analyzed in cell cycle checkpoint contexts. Wip1 preferentially targets multiple proteins at their pSQ/pTQ motifs, which are phosphorylated by ATM, ATR, or DNA-PK. In addition, Wip1 also targets pTXpY motifs in p38 mitogen-activated protein kinase (MAPK), which activates p53 upon DNA damage, and in the uracil DNA glycosylase UNG2, which regulates base excision repair (BER; Lu et al., 2004; Takekawa et al., 2000). Wip1 has also been reported to facilitate the reversal of cell cycle checkpoint responses, returning cells to the homeostatic state after completion of DNA repair. Wip1 likely plays a role in the p53 negative feedback loop through two pathways, i.e., dephosphorylation of p38 or p53. Following DNA damage, p53 up-regulates Wip1, which then inhibits p38 via dephosphorylation at T180; inactivated p38 results in inhibition of p53 (Bulavin et al., 1999; Appella and Anderson, 2001). On the other hand, up-regulation of Wip1 reverses p53 activation by dephosphorylating p53 at S15 (Lu et al., 2005). UNG2, another target of Wip1, is phosphorylated and activated in response to UV, inducing BER activity. Wip1 also inhibits BER activity through dephosphorylation of UNG2 at T6 after completion of DNA repair (Lu et al., 2004). Importantly, mice lacking Wip1 are viable but exhibit defects in reproductive organs, immune functions, and cell cycle control (Choi et al., 2002). Knockout of Wip1 triggers p38-mediated activation of the p53, p16, and p19 pathways, leading to enhanced DDRs, promoting genomic stability, and providing resistance to transformation by oncogenes (Bulavin et al., 2004). Consistent with Wip1's function as an oncogene, amplification of this gene has been reported in several human tumors, including breast cancer, neuroblastoma, and ovarian clear cell adenocarcinoma (Bulavin et al., 2002; Li et al., 2002; Hirasawa et al., 2003; Saito-Ohara et al., 2003). In fact, an associated checkpoint phenotype was reported; overexpressed Wip1 cells abrogated S phase and G_2/M DNA damage checkpoints, whereas reduction of Wip1 expression

enhanced the enforcement of intra-S and G_2/M checkpoints (Lu et al., 2005).

PPM1G

PPM1G (also denoted PP2Cγ), a PP2C phosphatase what was originally identified as a splicing factor, has a role in the DDR. PPM1G mediates the exchange of H2A-H2B, which is implicated in the recovery from DNA damage (Kimura et al., 2006). PPM1G-knockdown cells show defects in normal cell proliferation (Allemand et al., 2007), and PPM1G-deficient DT40 cells are sensitive to DNA damage (Kimura et al., 2006), indicating the important role of PPM1G in cell growth and the DDR. Recently, another report demonstrated that PPM1G has a new function in p53 activation through the deubiquitinating enzyme USP7 (also known as HAUSP), which stabilizes the E3 ligase Mdm2 (Khoronenkova et al., 2012). In fact, following IR, ATM phosphorylates and activates PPM1G, which then dephosphorylates and inactivates USP7, leading to Mdm2 degradation and accumulation of p53.

DDR PLAYERS ARE DEPHOSPHORYLATED BY PROTEIN PHOSPHATASES

SENSOR KINASES, ATM, ATR, AND DNA-PK

PP2A

PP2A has been reported to operate as a regulator of ATM (Goodarzi et al., 2004). In the absence of DNA damage, PP2A associates with and dephosphorylates ATM at S1981 (**Figure 1A**). Following DNA damage, rapid dissociation of PP2A from ATM leads to activation of ATM. Inhibition of PP2A by OA or by expressing a dominant-negative mutant of PP2Ac induces autophosphorylation of ATM at S1981 in undamaged cells without activation of ATM activity (Yan et al., 2010). Other reports demonstrated that IR induces dissociation of the B55 subunit from PP2A in an ATM-dependent manner, influencing the disruption of ATM-PP2A (Guo et al., 2002). Despite these studies, the molecular mechanism regulating the dissociation of ATM-PP2A remains to be determined.

Little is known about the role of PP2A in mediating DNA-PK. Studies have shown that the interaction of PP2A with the DNA-PK subunits Ku70 and Ku80 is induced by DSBs. Moreover, PP2A has been shown to dephosphorylate each of these proteins both *in vitro* and *in vivo* (**Figure 1C**). Further functional analyses showed that PP2A-dependent dephosphorylation of DNA-PK subunits enhances the formation of a functional DNA-PK, leading to promotion of NHEJ and DSB repair (Douglas et al., 2001; Wang et al., 2009).

PP1

PP1-dependent DDR regulation is partly mediated by its chromatin targeting subunit, Repo-Man, which was isolated as a PP1γ-specific interacting protein (Trinkle-Mulcahy et al., 2006; Vagnarelli et al., 2006). Studies in *Xenopus* egg extracts demonstrated that Repo-Man interacts with ATM and PP1 through distinct domains, leading to PP1-dependent regulation of ATM phosphorylation and activation (Peng et al., 2010; **Figure 1A**). Following DNA damage, the Repo-Man-PP1γ complex is released from chromatin, leading to activation of ATM at DNA damage sites.

Wip1

Wip1 suppresses ATM activity through dephosphorylation of ATM, resulting in restoration of ATM to its dephosphorylated state after completion of DNA repair (Shreeram et al., 2006; **Figure 1A**). Given the fact that Wip1 is constitutively associated with ATM, how Wip1 activity is regulated remains to be determined.

PP5

Unlike the phosphatases described above, PP5 has a role in the activation of ATM and the association between ATM and PP5 is induced by DNA damage (Ali et al., 2004). Following DSBs, ATM-mediated phosphorylation of Rad17 at pS635 and p53 at S15 is not induced in PP5-knockdown cells, which exhibit an impaired S-phase checkpoint (Ali et al., 2004). In fact, expression of a catalytically inactive PP5 mutant inhibits ATM activation, whereas wild-type PP5 does not affect the phosphorylation status of ATM at S1981 after IR exposure (Ali et al., 2004; Wechsler et al., 2004). These results suggest that PP5 is likely not involved in dephosphorylation of this site, but instead may be involved in the activation of ATM (**Figure 1A**).

Regulatory links between PP5 and ATR as well as PP5 and ATM have been demonstrated (Zhang et al., 2005). PP5 interacts with ATR in a DNA damage-dependent manner, and down-regulation of PP5 leads to defects in the phosphorylation of ATR targets, including Rad17 and Chk1, following UV or HU and an aberrant S-phase checkpoint, indicating the involvement of PP5 in ATR activation (**Figure 1B**). Whether ATR is a substrate of PP5 currently remains unknown.

PP5 interacts with and dephosphorylates DNA-PKcs (Wechsler et al., 2004; **Figure 1C**). Phosphorylation of DNA-PKcs at T2609 and S2056 is reduced in cells overexpressing PP5, suggesting that PP5 mediates dephosphorylation of DNA-PKcs.

PP6

DNA-PKcs associate with PP6 and all regulatory subunits, including PP6R1, PP6R2, and PP6R3, and PP6 is involved in dephosphorylation of DNA-PKcs (Mi et al., 2009b; Douglas et al., 2010; **Figure 1C**). IR enhances this interaction and promotes the import of this complex into the nucleus (Mi et al., 2009b). In contrast, other findings have indicated that the interaction between DNA-PKcs and the PP6 complex is constitutive (Douglas et al., 2010). Although it is not clear whether the interaction between DNA-PKcs and PP6 is indeed induced by DNA damage, Douglas et al. (2010) produced an attractive model in which DNA-PKcs recruit PP6 complexes to damaged sites, permitting PP6 to contribute to the dephosphorylation of H2AX, dissolution of foci, and release from the G_2/M checkpoint.

BAAT1

BRCA1-associated protein required for ATM activation 1 (BAAT1), which was isolated as a BRCA1-interaction partner, is important for activation of ATM (Aglipay et al., 2006; **Figure 1A**). Expression of BAAT1 and association of BAAT1 with ATM are increased after IR. Importantly, phosphorylation of several ATM targets, including H2AX, NBS1 at S343, Chk2 at T68, and ATM

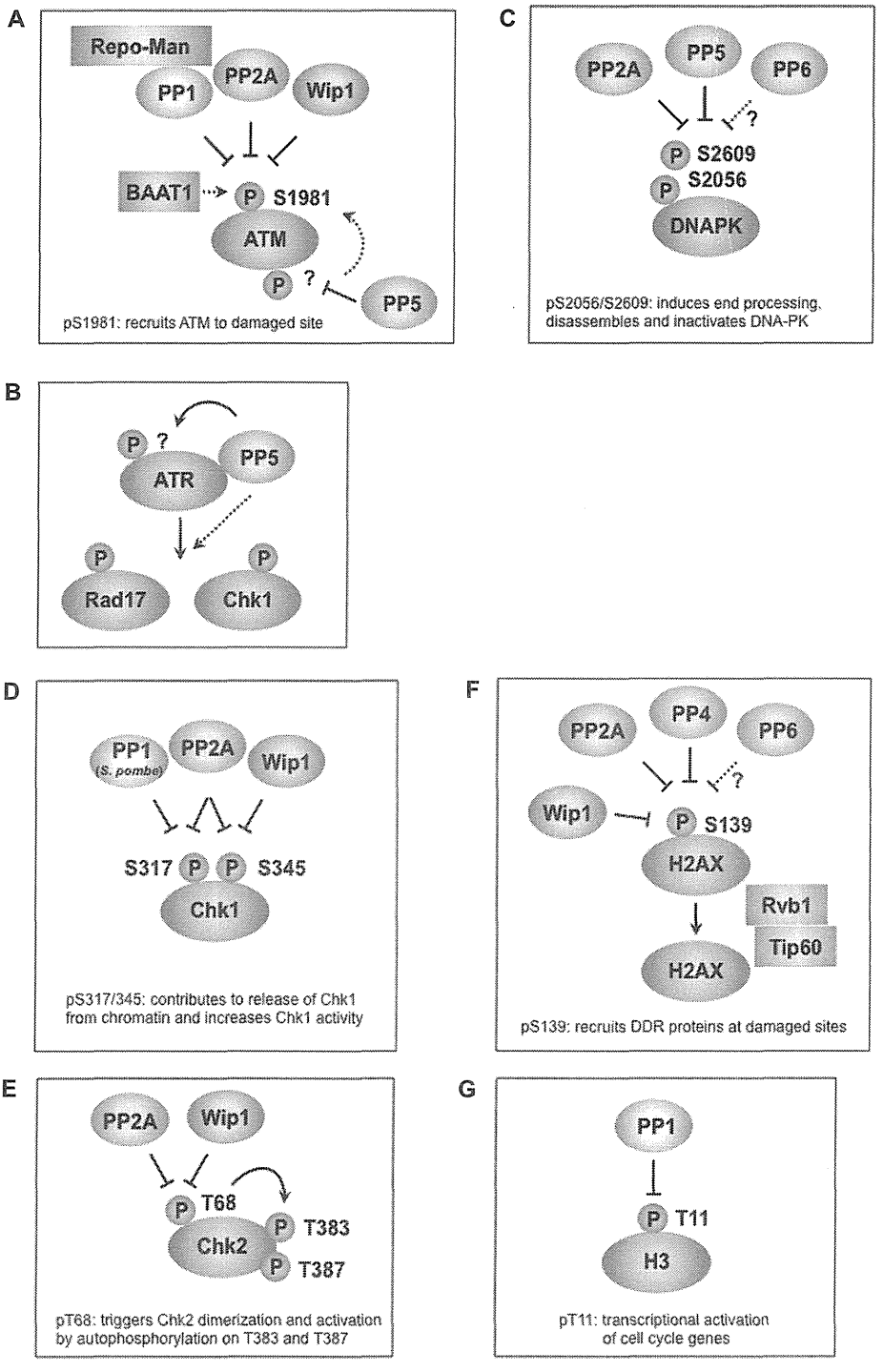

FIGURE 1 | Protein phosphatases regulate multiple phosphorylation events in the DNA damage response. (A) PP1, PP2A, and Wip1 dephosphorylate ATM at S1981, which is required for the recruitment ATM to damage sites. BAAT1 protects ATM from dephosphorylation by phosphatases. PP5 is likely involved in ATM activation through dephosphorylation of ATM, which may induce ATM phosphorylation at S1981. **(B)** PP5 is required for ATR- targeted phosphorylation of Rad17 and Chk1. Although PP5 associates with ATR in a DNA damage-dependent manner, the precise mechanism remains to be determined. **(C)** PP2A, PP5, and possibly PP6 dephosphorylate multiple sites on DNA-PK, including S2056 and S2609. These sites are autophosphorylated by DNA-PK and are involved in the activation/inactivation of DNA-PK. **(D)** PP1 (*S. pombe*), PP2A, and Wip1 dephosphorylate Chk1 at S317 and/or S345, which promotes its release from chromatin and increases Chk1 kinase activity. **(E)** PP2A and Wip1 mediate the dephosphorylation of Chk2 at T68, which facilitates Chk2 dimerization and

(Continued)